Journal of Archaeological Science: Reports 70 (2026) 105607

Contents lists available at ScienceDirect

Journal of Archaeological Science: Reports

journal homepage: www.elsevier.com/locate/jasrep

Decoding Sumerian craft technologies: morphological image processing and mesoscopic feature analysis of archaeological bitumen-based composites

V. Caruso [a,b,*], C. Scatigno [a,**], S. Giampaolo [a], A. Tufari [c], L. Ferguson [c], F. Manclossi [c], A. Greco [c,d], L. Romano [c,e], G. Festa [a,**]

[a] CREF – Museo Storico della Fisica e Centro Studi e Ricerche "Enrico Fermi", via Panisperna 89, 00184 Rome, Italy
[b] Università degli Studi di Roma Tre, Dipartimento di Studi Umanistici, Via Ostiense 236, 00144 Rome, Italy
[c] Dipartimento Istituto Italiano di Studi Orientali, Sapienza Università di Roma, Piazzale Aldo Moro 5, 00185 Rome, Italy
[d] Gerda Henkel Stiftung, Malkastenstraße 15, 40211 Düsseldorf, Germany
[e] School of Historical and Philosophical Studies, University of Melbourne, Arts West Building, Arts West – North Wing, Royal Parade, Parkville, VIC 3010, Australia

ARTICLE INFO

Keywords:
Two-dimensional image processing analysis
Machine learning algorithms
Pore fraction
Vegetal additives
Inorganic inclusions
Bitumen-based composites
Sumerian material practices
Archaeological sustainability

ABSTRACT

This study introduces an innovative, reproducible, non-destructive and non-invasive analytical protocol that combines two-dimensional digital microscopy with machine learning to investigate the mesostructure of archaeological bitumen-based composites from the Sumerian site of Abu Tbeirah (Iraq). A total of 59 samples were analysed, including residues on tools and ceramics, spherical objects, standardised ingots likely used for storage or trade, and unidentified fragments.

The custom image analysis protocol was developed to extract and quantify morphological and morphometric features of the bitumen-based samples, including pore structures, vegetal and inorganic additives, and inclusions, revealing details about raw material selection, recipes' composition, and working procedures. Statistical analyses, including Classical and Robust Principal Component Analysis, highlighted distinct technological patterns associated with specific functional uses, such as adhesives, coatings, waterproofing agents, and glues. The variability observed among artefacts differentiates the *chaînes opératoires* and suggests specialised knowledge in material preparation and reuse, consistent with broader evidence of craft specialisation and resource management in the late third millennium BCE southern Mesopotamia.

Parallels with modern bitumen processing techniques point to long-term continuity in material innovation and sustainable technological practices. This research demonstrates that the integration of imaging techniques, computational analysis, and archaeological interpretation can elucidate ancient technological systems, offering a methodological framework for future studies of composite materials in archaeology.

1. Introduction

Bitumen played a significant role in the economic and political development of the Sumerian population in ancient Mesopotamia, as evidenced by several bitumen-related terms preserved in cuneiform tablets (Stol, 2012). The use of this material by human societies has deep prehistoric roots. Evidence from Umm el Tlel and Hummal in Syria, based on lithic artefacts and flakes, indicates that human hunter-gatherer societies exploited natural bitumen as early as Middle Palaeolithic (approximately 70,000 BP), likely for its adhesive and protective coating properties (Boeda et al., 2008; Hauck et al., 2013).

From the Bronze Age onward, bitumen was extensively extracted from natural sources—in both liquid and solid form—in the Near East and subsequently distributed throughout key Mediterranean regions, including Italy and Egypt (Schwartz and Hollander, 2016; Connan et al., 2018; Breu et al., 2022). This fossil resource served multiple purposes in

* Corresponding author at: CREF – Museo Storico della Fisica e Centro Studi e Ricerche "Enrico Fermi", via Panisperna 89, 00184 Rome, Italy.
** Corresponding author.
E-mail addresses: caruso.valentina87@gmail.com, val.caruso10@stud.uniroma3.it (V. Caruso), claudia.scatigno@cref.it (C. Scatigno), silvia.giampaolo@cref.it (S. Giampaolo), tufari.2053996@studenti.uniroma1.it (A. Tufari), ferguson.2078438@studenti.uniroma1.it (L. Ferguson), greco_angela@hotmail.it (A. Greco), licia.romano@unimelb.ed.au (L. Romano), giulia.festa@cref.it (G. Festa).

https://doi.org/10.1016/j.jasrep.2026.105607
Received 27 October 2025; Received in revised form 22 December 2025; Accepted 24 January 2026

Sumerian daily life owing to its adhesive, waterproofing, antiseptic and ignition properties (Connan et al., 2005; Fulcher and Budka, 2020; Ferrant et al., 2022; Connan et al., 2008; Connan et al., 2006; Nissenbaum et al., 2002; Oxilia et al., 2017; Dutoit et al., 2022).

The transformation of raw bitumen into functional materials involved sophisticated processing techniques. To achieve the desired viscosity, enhance its properties and extend available supplies, natural bitumen was heated and melted in jars over a fire and mixed with both vegetal debris (e.g., plant, straw, and reeds) and inorganic materials (e.g., minerals, powdered pottery, and shell fragments). These additions served multiple purposes: lowering the melting point, increasing mechanical strength, and boosting volume. Both the melting and mixing processes fundamentally altered the physicochemical properties of bitumen, making it suitable for a wide range of applications (Boeda et al., 2008).

For storage and trade, bitumen—either in raw or processed form—was moulded into standardised blocks, the so-called ingots, which were often covered with pieces of reed mats to facilitate handling and prevent adhesion (Connan et al., 1998; Connan et al., 2018). Owing to the complex and resource-intensive nature of this production process, bitumen-based composites were often recycled into lower-grade materials. Written sources attest to the reuse of bitumen collected from decommissioned boats, while archaeological evidence further suggests its collection from production waste, broken ceramics and tools (Greco et al., forthcoming; Verderame 2025). However, extensive reheating made these composites excessively hard and brittle for practical use (Schwartz and Hollander, 2000).

Traces of each production stage are preserved in the final product, and manufacturing processes can differ significantly depending on the intended application. The number of heating cycles, combined with the presence of authigenic materials—either deliberately added during manufacturing or accidentally incorporated during geological formation—are key factors in determining both the processing methods employed and the geographical origin of the bitumen (Schwartz and Hollander, 2008; Koyun et al., 2021).

Reference studies on ancient bitumen have predominantly focused on examining complex hydrocarbon mixtures through molecular and isotopic analyses (Connan et al., 2018; Breu et al., 2022; Connan et al., 2024; Cosac et al., 2013; Cârciumaru et al., 2012). While these approaches have successfully identified chemical compositions and geographical origins, comparatively few studies have investigated the structural characteristics of bitumen-based composites. Microscopic analysis has typically been employed only as a preliminary technique to evaluate gross morphological properties (Breu et al., 2017; Connan and Oates, 2018; Connan et al., 2006; Connan et al., 2013).

In contrast, studies focusing on high-resolution digital imaging have been widely conducted on modern asphalt pavements in engineering applications (Jing et al., 2023; Taheri-Shakib 2023; Middendorf et al., 2023), but comparable systematic approaches have not been extensively applied to archaeological bitumen-based composites.

To improve our understanding of the physical *chaîne opératoires* (processing and recycling) of ancient craftsmen, the present study examined 59 bitumen-based composites from the Sumerian settlement of Abu Tbeirah in southern Iraq, dated to the late third millennium BCE (Romano and D'Agostino, 2019), using a two-dimensional digital image processing technique. The applied methodology allows for the direct visualization and quantification, in a reproducible, non-destructive, and non-invasive way, of the mesostructure of bitumen-based composites.

The analytical strategy employed automated image investigation to extract information about morphological features—including pores, vegetal and inorganic materials—and their related morphometric metrics, including size, shape, density, and spatial distribution, from a set of images acquired using a digital microscope. To preserve sample integrity, a specific protocol for preparation and analysis was implemented. The internal portions of the bitumen-based composite samples were carefully exposed to avoid surface contamination and directly examined under optical microscopy.

A custom Python-based pipeline was developed to perform quantitative morphological analysis from binary and grayscale TIFF images, extracting geometric features with automated binarization. This ongoing research has significant archaeological implication within the framework of the SLOW SUMER project, as it sheds new light on how bitumen-based composites were obtained, processed, sorted, redistributed, and used within the Sumerian culture.

2. Materials

2.1. Archaeological context

Abu Tbeirah is a Sumerian settlement located in the southern Iraqi province of Dhi Qar, within the historically oil-rich Al-Rafidayn region. The site was occupied from the Early Dynastic Period (c. 2900–2350 BCE) until the decline of the Ur III Dynasty (c. 2000 BCE). Strategically sited near major Mesopotamian cities such as Ur, Abu Tbeirah played a key role in regional trade and communication networks.

Positioned within the Mesopotamian floodplain, the site once lay near the ancient Euphrates delta and the reconstructed coastline of the Persian Gulf (Fig. 1a). Although the location is prone to salinisation and erosion, due to its proximity to ancient marshlands, excavations have revealed a well-planned urban settlement of 43 ha at 4 m above sea level. Notable features include mudbrick architecture and sophisticated hydraulic infrastructure, such as canals and an artificial harbour (Fig. 1b).

Of particular interest in the southeastern part of the tell (Area 1) is Building A, a multifunctional household structure that, in the two phases excavated so far, served both domestic and craft-related activities. Within this complex, Phase 1 – Room 23 (Fig. 1c) was specifically used for melting and decanting bitumen, as indicated by the presence of vessels near a fireplace and by the large quantity of bitumen artefacts recovered. Heavy residue analysis of the pavement further indicates that the southeastern corner of the room functioned as a storage area, supported by the presence of ingots and discarded object fragments likely intended for recycling (Cereda, 2019). In the earlier phase (Phase 2) of the same room, a pit excavated beneath the floor revealed a concentration of bitumen-based objects, possibly representing a form of storage, which suggests continuity in the use of the space. These findings point to practices of maintenance and reuse, indicating a sustained management of bitumen resources over time. Marking the final phase of Area 1 occupation, a cemetery containing numerous burials was identified just beneath the surface (Romano and D'Agostino, 2019; Festa et al., 2025).

Additional samples derive mainly from Area 4 and Area 6, located in the northeastern quadrant of the site. Area 4 yielded evidence of a building (Building D), interpreted as a domestic structure. Two phases have been identified, although the latest phase was almost completely eroded. While Phase 2 was deliberately emptied prior to abandonment, its architectural layout and functional characteristics are comparable to those of Building A in Area 1, supporting its interpretation as a household context. Area 6 is characterised by the presence of two phases of an Ur III structure, Building E, whose latest phase is preserved only through its brick foundations. Among the bricks, one bearing the name of Amar-Suena was recovered, indicating that the latest phase of the building belonged to an elite architectural context and can be securely dated to the Ur III period. The earlier phase of the building has only been partially investigated, as its rooms were heavily disturbed by the later foundations. The remains of this structure were subsequently cut by several graves, which appear to belong to a later cemetery phase (Romano and D'Agostino 2023).

2.2. Sample description

The present analysis examined 59 archaeological bitumen-based

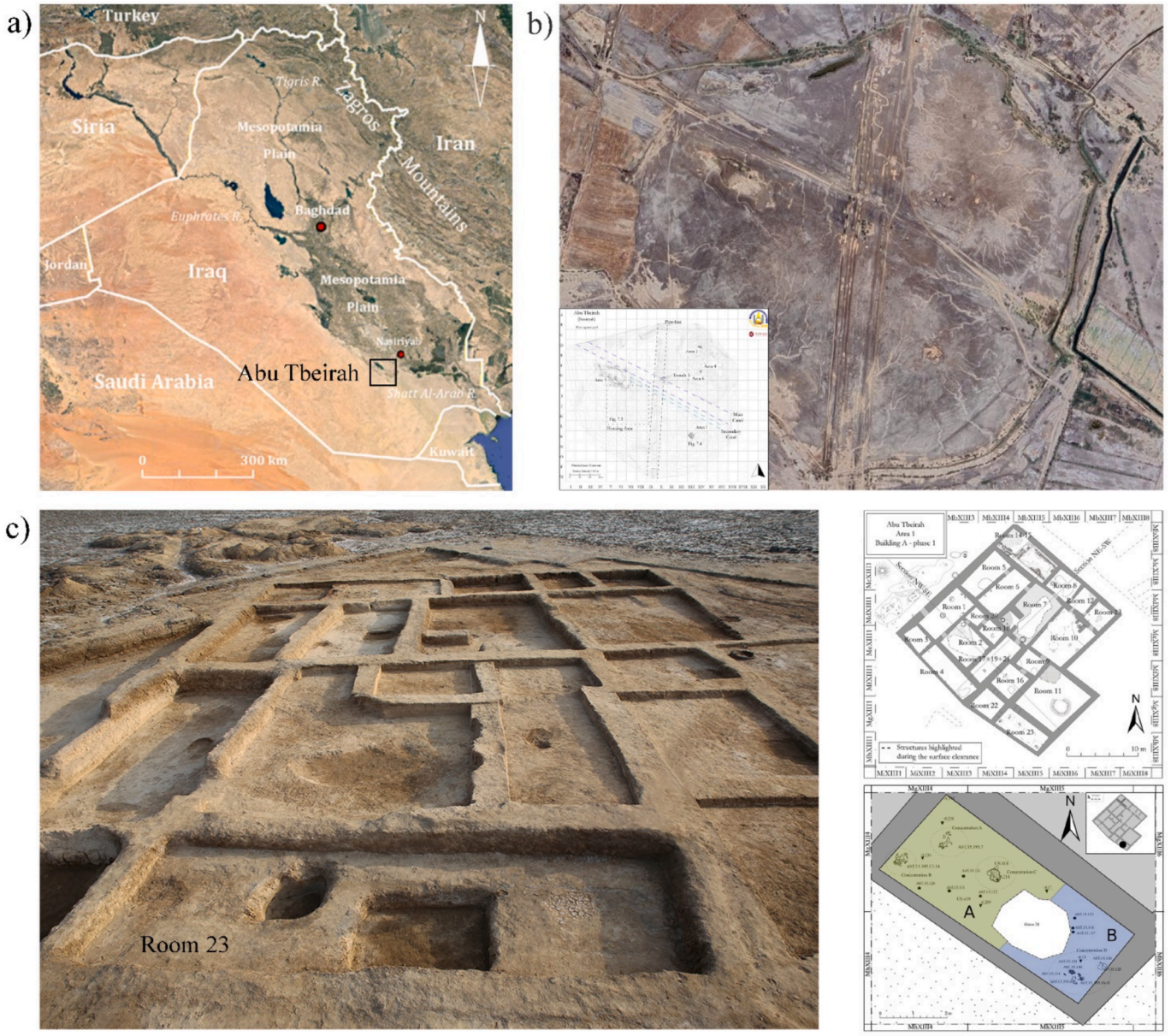

Fig. 1. a) Geographical map of Iraq showing the location of the Abu Tbeirah settlement; b) Overview of the Abu Tbeirah archaeological site, indicating the areas where the bitumen-based composite samples were collected; c) detail of building a in area 1, with room 23 identified as a bitumen workshop (images adapted from Romano and D'Agostino, 2019).

composites from the Abu Tbeirah site, representing all well-preserved specimens suitable for non-destructive mesostructural analysis recovered from multiple stratigraphic units and contexts during excavation campaigns (Table 1). This assemblage provides a representative understanding of bitumen use at the site during the late third millennium BCE.

The bituminous nature of the samples has been confirmed through chemical profiling using Fourier Transform Infrared Spectroscopy (FTIR), with results published in Festa et al. (2025). The study identified the characteristic bitumen fingerprint through distinctive hydrocarbon features: a double-band pattern at 3000–2700 cm^{-1} associated with aliphatic C–H stretching (2950–2850 cm^{-1} for CH_2 and CH_3 groups), and absorption in the 1100–1500 cm^{-1} range associated with aliphatic deformation (C–H bending at 1460–1375 cm^{-1}). Aromatic group vibrations were identified through C═C stretching at 1600 cm^{-1} and C═C rocking at 860–700 cm^{-1}. Additionally, signs of ageing were indicated by O–H stretching bands at 3300–3400 cm^{-1} from intermolecular hydrogen bonding, while carbonate and silicate contributions at 875 and 1057 cm^{-1} reflected the composite nature of these archaeological materials. Given this chemical complexity, the term 'bitumen-based composite' has been adopted to describe the studied samples, acknowledging their heterogeneous composition of a hydrocarbon bitumen matrix incorporating both environmental contaminants and intentional vegetal/mineral fillers.

Based on a combination of morphological characteristics (texture, colour, and density), composition (vegetal/inorganic materials), and archaeological context (location and associated artefacts), archaeologists classified the specimens into four functional typologies:

1) *Residues and Traces* (Fig. 2a, c, d, e, f): bitumen composites adhering to or coating objects, including grinding stones, pottery, sarcophagi, reed mats, wicker baskets, and chipped stone tools. These specimens preserve direct evidence of functional applications.

Table 1
Distribution of the 59 bitumen-based samples by typology, provenance and context.

	ID Sample	Total
Typology		
1 – Residue/Trace on flint sickle blade, grindstone, bitumen-based container, sarcophagus, reed mat, reed woven basket, pottery	7, 28, 33, 44, 51, 53, 55, 58, 65, 67	10
2 – Unidentified fragment	9, 10, 11, 13, 14, 17, 19, 20, 21, 22, 23, 24, 25, 26, 27, 31, 32, 34, 35, 36, 38, 45, 46, 48, 57, 59, 60, 61, 62, 63, 66, 68, 69	33
3 – Spherical object	8, 16, 18, 29, 30, 37, 39, 40, 41, 43, 64	11
4 – Ingot	12, 42, 50, 52, 54	5
Provenance		
Area 1 – Cemetery	48, 51, 52, 53, 58, 59, 60, 61, 62, 63, 64	12
Area 1 – Building A	8, 10, 11, 12, 16, 18, 20, 21, 23, 24, 25, 28, 29, 30, 31, 34, 35, 36, 37, 38, 39, 40, 41, 43, 44, 45, 46, 50, 54, 55, 57, 66, 67, 68	34
Area 2 – Cemetery	17	1
Area 4- Surface	19	1
Area 4 – Building D	7, 13, 14, 22, 26, 27, 65, 69	8
Area 6- Surface	32	1
Area 6 – Building E	9, 33, 42	3
Context		
Area 1 – Building A – Phase 1 – Workshop	11, 18, 20, 55, 57, 66	6
Domestic (All Areas)	7, 8, 9, 10, 12, 13, 14, 16, 21, 22, 23, 24, 25, 26, 27, 28, 29, 30, 31, 33, 34, 35, 36, 37, 38, 39, 40, 41, 42, 43, 44, 45, 46, 50, 54, 65, 67, 68, 69	39
Funerary	17, 51, 52	4
Funerary/Workshop (in the backfill of Grave 23, cutting the workshop's layers)	53, 58, 59, 60, 61, 62, 63, 64	8
Unknown	19, 32	2

2) *Unidentified Fragments* (Fig. 2h): lumps of uncertain function with no clear association with specific objects. These may represent production waste, degraded artefacts, or decontextualised fragments from various applications.
3) *Spherical Objects* (Fig. 2g): artefacts composed entirely of bitumen-based composites, whose precise function remains uncertain. These objects with drop-like and rounded morphologies may have served as probable storage units to facilitate trade and exchange or functioned as raw material ready for reprocessing (Connan et al., 2008; Pinto et al., 2019).
4) *Ingots* (Fig. 2b): standardised blocks of processed bitumen-based composites (i.e. bitumen with vegetal and mineral additives) representing semi-finished products intended for storage and transportation. These specimens often preserve impressions of reed mats on which they were placed to dry after heating and melting, providing direct evidence of production techniques (Connan et al., 1998).

Detailed information on each sample—including provenance, archaeological context, and functional classification—is provided in Supplementary Table S1.

2.3. Bitumen provenance, composition and manufacturing

Bitumen from Hit (central Mesopotamia) was the dominant source along the Euphrates, although other supply networks from southwestern Iran as well as central and northern Mesopotamia were also exploited (Connan and Van de Velde, 2010). Based on established regional trade patterns, historical texts, and Abu Tbeirah's geographical position, the bitumen-based composite examined here likely originated from the petroleum-bearing region of Hit–Ramadi–Abu Jir (Fig. 1a), although an eastern provenance (Iran) cannot be entirely excluded. Samples from Abu Tbeirah are currently undergoing biomolecular and isotopic analyses in order to define their specific origin. All specimens display evidence of similar diagenetic processes, primarily salinisation and erosion, consistent with the site's location within ancient marshland environments.

Sumerian bitumen-based composites are the final product of a complex, multi-stage manufacturing process, resulting in a black, viscous, semi-solid, and porous material, composed of natural petroleum combined with various additives and inclusions. The internal components fall into two primary categories, each contributing distinct properties to the final composite.

Vegetal material—such as plant debris, straw, and reed fragments—were predominantly added intentionally to modify the consistency and functionality of natural bitumen. However, these materials may also appear as incidental traces, resulting from handling or drying processes, including impressions left by reed mats and baskets during production or transport (Connan et al., 2006; Connan et al., 2013; Connan and Oates, 2018). The inorganic material consisted of powdered minerals, fragmented rock, shells, and ceramic debris. These components exhibit more varied origins: some were deliberately incorporated during preparation to enhance mechanical properties, while others derived from the sedimentary matrix, surrounding archaeological context, or were introduced through wear and abrasion of tools to which the composite was applied (Breu et al., 2017; Boeda et al., 2008; Connan et al., 2013).

The internal composition directly influences the mesostructure and physicochemical properties of the material examined. In this study, mesostructure refers to the internal architecture at an intermediate observational scale—between macrostructure (visible either to the naked eye or at low resolution) and microstructure (observable at microscopic, crystalline, and molecular levels). Image analysis at the mesoscale focuses on identifying and quantifying spatial heterogeneities, discrete aggregates, surface morphologies, and textures that influence physical, mechanical, and visual properties. Rather than being defined by absolute dimensional boundaries, mesostructure is characterised by its functional relevance in linking elemental composition to emergent bulk-scale properties (Crabtree et al., 2012), with typical features ranging from tens of micrometers to several millimeters.

3. Methods

To characterise pore distribution and quantify the relative abundance of vegetal and inorganic materials in bitumen-based composite samples, an eight-step methodology was developed (Fig. 3a).

Step 1 – Sample Preparation: to preserve the integrity of bitumen-based composites and minimise contamination from environmental sources (e.g. soil, moisture, human activity, or biological agents), a clean sampling protocol was carried out. An incision was made on the external surface of each specimen using a sterile surgical scalpel, held parallel to the sample's flat face, following the natural cleavage plane as closely as possible. This controlled cut bisected the sample, exposing a fresh inner portion. This newly revealed inner piece of sample, isolated from surface contamination, was subsequently examined under a digital microscope. This procedure ensured that the microscopic analysis was conducted on uncontaminated, structurally representative material while acknowledging the inherent heterogeneity of archaeological bitumen-based composites.

The workflow of the methodology employed, from sample preparation to identification and extraction of features of interest (pores, vegetal and inorganic materials) through image analysis, is exemplified by sample 18 in Fig. 3b.

Step 2 – Microscopic analysis: the analysis was performed using a Jiusion USB digital microscope (maximum magnification: 1000×;

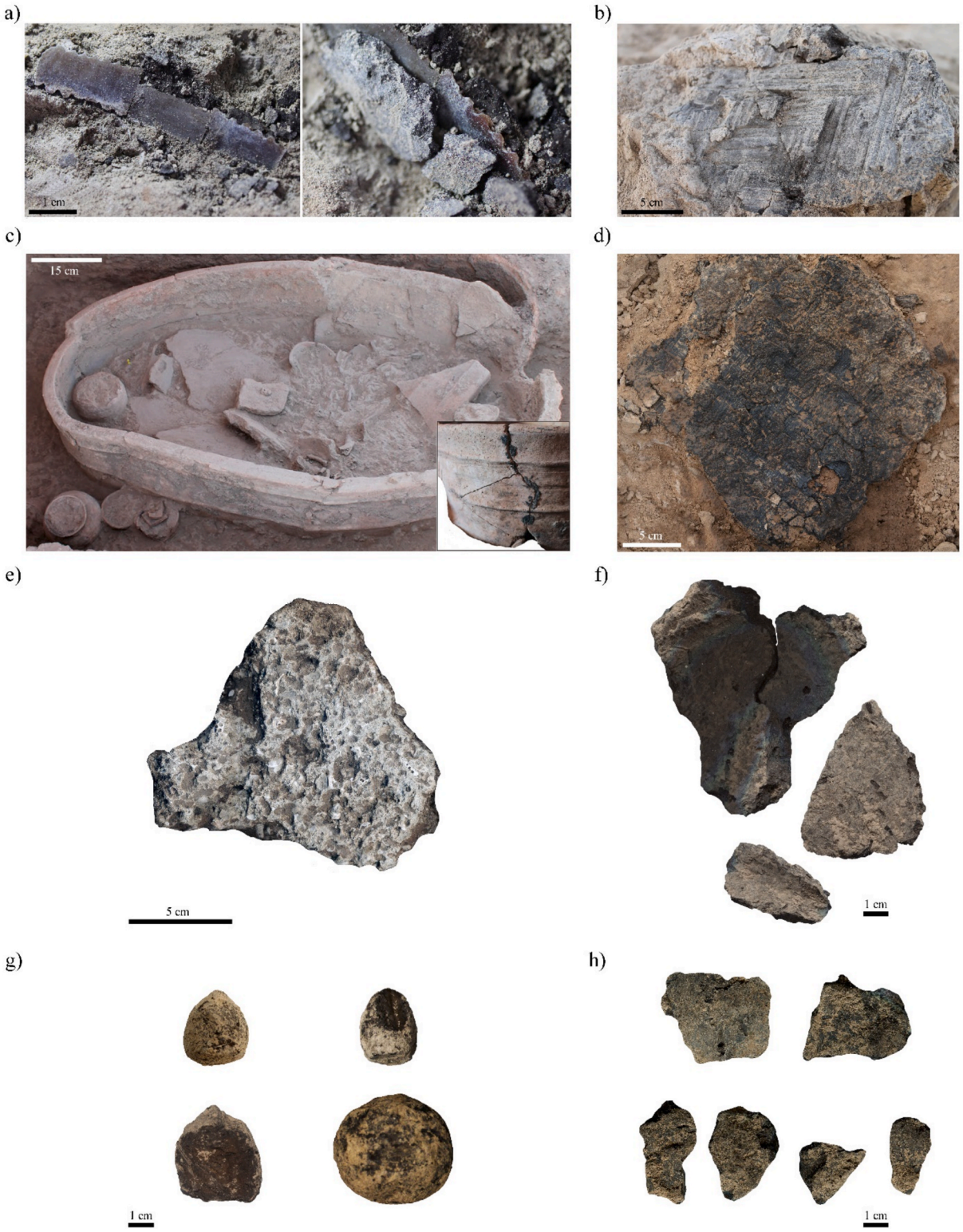

Fig. 2. Representative examples of bitumen-based composite typologies identified through archaeological analysis. Samples are shown in their as-found condition with outer surfaces still bearing adherent soil particles: a) Residue adhering to the haft of a flint sickle blade; b) Ingot, a standardised block displaying parallel diagonal lines from reed mat impressions on the surface; c) Residue on a sarcophagus rim used for structural repair; d) Reed-woven basket coated with bituminous material; e) Residue on a grindstone surface; f) Fragments with preserved rims and intentionally shaped concave surfaces of small vessels made with bitumen; g) Spherical objects exhibiting drop-like and rounded morphologies; h) Unidentified fragmentary remains.

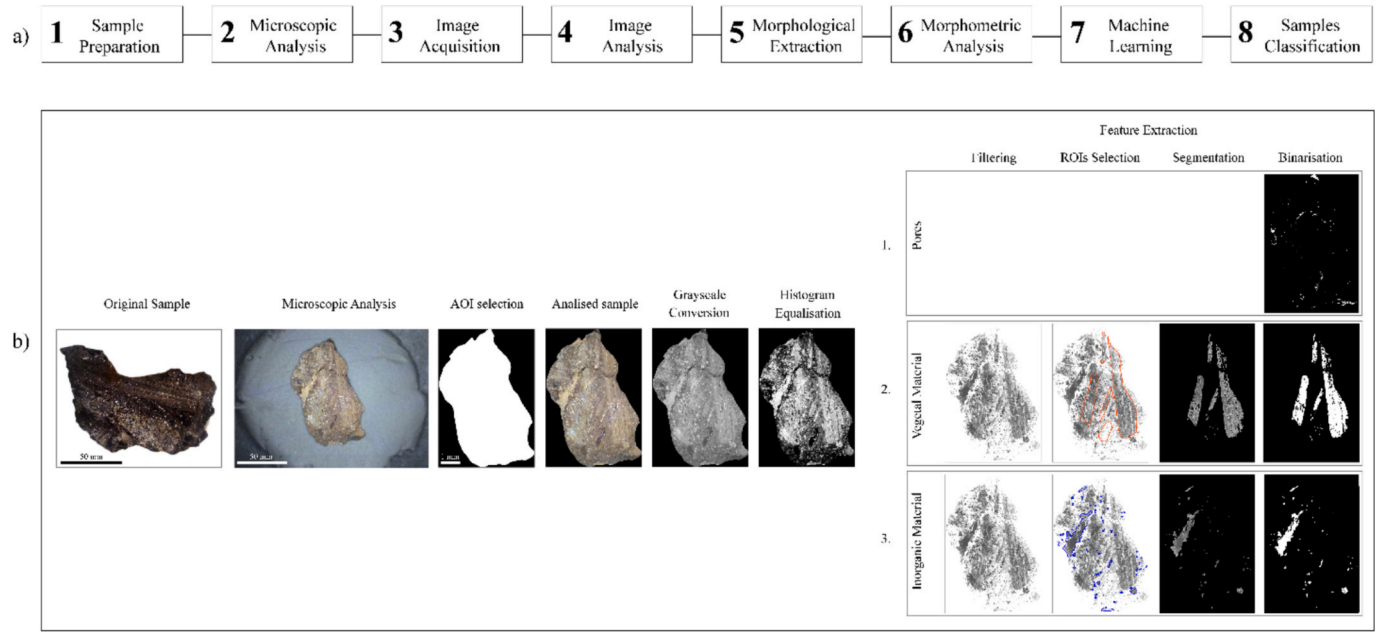

Fig. 3. a) Step-by-step analytical protocol for mesostructural characterisation of bitumen-based composites, from sample preparation to quantitative analysis, including imaging, processing, and data extraction. b) Workflow for extracting features of interest (pores, vegetal and inorganic materials), exemplified through sample 18. The fresh inner portion for analysis was obtained by sectioning, to isolate the analysed sample from raw surface contamination and examined under digital microscope. Following image acquisition, the area of interest (AOI) was selected by cropping the outer border of the sample; non-sample areas were filled with black pixels (0 intensity value) to establish a standardised background. Pre-processing steps, including conversion to 8-bit grayscale format and histogram equalization (HE), were then applied. From the equalised image, three pipelines were employed for feature extraction. Pipeline 1 involved direct extraction of pores through binarization; Pipelines 2 and 3 applied a denoising process using a Retinex-based filtering algorithm and a 3 × 3 median filter, followed by manual selection of regions of interest (ROIs) containing vegetal and inorganic materials, where segmentation was exclusively performed.

resolution: 1920 × 1080 pixels). The following protocol was implemented to ensure image quality and consistency:

a) samples were positioned to achieve maximum surface flatness and illuminated perpendicularly to minimise shadowing effects.
b) the lighting system was calibrated to ensure uniform illumination across the entire surface.
c) for optimal imaging conditions, samples were mounted within a darkened chamber and illuminated exclusively by the microscope's calibrated internal light source.

This approach improved image consistency, reduced artefacts from reflection and shading, and minimised localised intensity variations that could compromise analytical accuracy.

Step 3 – Image Acquisition: RGB images were recorded using Xplotview software and saved in uncompressed TIFF format to preserve full image information for subsequent digital processing.

Step 4 – Image Analysis: image analysis was performed by combining both manual FIJI (Schneider et al., 2012) methods and automated custom Python scripts developed in PyCharm (JetBrains IDE, PyCharm, 2024). Image analysis pipeline included the following operations:

a) Area of Interest (AOI) selection: non-sample regions, including the positioning chamber and mounting fixtures, were manually excluded without altering the boundaries of the artefact itself. The AOI was cropped from the outer borders, and all non-sample areas were filled with black pixels (intensity value = 0) to establish a standardised background.
b) Image rescaling: to enable quantitative inter-sample comparisons, all AOI images were rescaled to a standardised dimension of 845 × 767 pixels using bilinear interpolation.
c) Grayscale conversion: rescaled images were converted to 8-bit grayscale format, with black non-sample areas assigned an intensity value of 0.
d) Histogram Equalization (HE): adaptive HE was applied to enhance contrast in the composite matrix. Because HE can introduce artefacts, amplify noise, and alter local brightness—potentially distorting pore morphology (Yoo et al., 2012)—its effects were assessed through both visual inspection and quantitative metrics: entropy, Structural Similarity Index (SSIM), Laplacian sharpness, and Root Mean Square (RMS) contrast.

This approach demonstrates effective contrast enhancement with minimal information loss: entropy decreased slightly, indicating reduced randomness in pixel intensity distribution. SSIM remained high, confirming strong structural preservation. RMS contrast increased, enhancing visibility of intensity differences in low-contrast areas; and Laplacian sharpness improved moderately, demonstrating sharpness enhancement without over-processing or distortion of original structures. These findings confirmed that HE successfully enhanced feature visibility while preserving pore morphology and structural fidelity.

e) Filtering: to improve the delineation of contours for both vegetal and inorganic materials—which exhibit varying grayscale intensities relative to the surrounding bituminous matrix—an iterative Retinex-based filtering algorithm was applied. This procedure employed a non-conventional application of the Retinex principle, functioning as an iterative structural filter rather than a standard contrast enhancement tool. To mitigate characteristic Retinex artefacts—particularly unnatural halo effects around high-contrast edges caused by over-exaggeration of light–dark transitions—the Gaussian filter width parameter (σ) was empirically calibrated to 10.

This relatively conservative value ensures localised illumination estimation while focusing noise suppression at a fine spatial scale. The choice minimises large-scale halo artefacts while prioritising the preservation of fine local structures over broad-field contrast enhancement. Iterative application (5 iterations) provided progressive, localised

smoothing that refined material contours, effectively functioning to enhance structural accuracy prior to segmentation.

A 3 × 3 median filter was subsequently applied to remove residual pixel-level artefacts (noise). Importantly, the objective of this pre-processing stage was not to maximise conventional image quality assessment (IQA) metrics, but rather to optimise feature discriminability within the composite matrix for subsequent automated segmentation. Quantitative evaluation, performed using established metrics including Entropy, Lightness Order Error (LOE), BRISQUE, and NIQE (Rasheed et al., 2022), revealed that while the Retinex filtering stage alone may degrade certain no-reference IQA scores (e.g., BRISQUE and NIQE), due to structural alterations introduced during localised denoising, the complete pre-processing pipeline ensures functionally superior output for accurate feature extraction from the complex bitumen-based composite matrix.

Step 5 – Morphological extraction: given the heterogeneous nature of the bitumen-based composite matrix, a hybrid segmentation strategy for Regions of Interest (ROIs) selection was implemented combining manual and automated approaches.

1. Pore segmentation: Void spaces (pores) were isolated using global thresholding (pixel intensity < 5), exploiting their consistently low pixel intensity values relative to the matrix and inclusions

2–3. Vegetal and inorganic materials segmentation: vegetal and inorganic materials were identified through manual contour selection, based on morphological features and optical contrast (i.e., variations in brightness, colour, and texture) relative to the surrounding matrix, followed by local adaptive thresholding (pixel intensity range: 5–200). This approach accommodated the variable grayscale characteristics of different materials within the composite matrix.

The pipelines for step 5 are documented and available in the repositories: https://doi.org/10.5281/zenodo.18007818 for pores, and https://doi.org/10.5281/zenodo.18007711 for vegetal and inorganic materials.

Step 6 – Morphometric analysis: quantitative morphological data were automatically extracted from the segmented features. The script performs the following sequential operations:

a) Image loading and binarization: each segmented image was loaded and analysed to verify binary format (pixel values restricted to 0 and 255). For non-binary images, Otsu's automatic thresholding was applied to generate binary masks (Ma & Yue, 2022). Three independent binary masks were produced from each sample, corresponding to: (i) pores, (ii) vegetal material, and (iii) inorganic material. Masks identifying pores, vegetal material, and inorganic material for each sample are presented in Supplementary Figs. S1-S12.
b) Contour detection and shape descriptor extraction: external contours were identified and for each detected feature multiple morphological descriptors were computed (Table 2), providing comprehensive quantification of size, shape and spatial distribution.

Two categories of morphometric descriptors were calculated:

a) Direct metrics (computed directly from image data):
- Total number of features: count of all discrete features within each category.
- Area (mm^2): calculated by converting pixel area to physical dimensions using a calibrated scale factor based on 72 DPI image resolution.
- Major and minor axis lengths (mm): derived from the minimum-area bounding rectangle fitted to each feature contour.

b) Derived metrics (computed from ratios of measured parameters):
- Aspect ratio: defined as the ratio of major axis to minor axis length.
- Density: number of features per unit sample area.
- Normalised area: proportional area occupied by each feature category relative to total sample area.

Table 2
Morphometric parameters extracted from image analysis.

Morphometric descriptors	Unit	Description
Direct metrics		
Total number of features	[–]	The total count of discrete features within a category
Area of feature	[mm^2]	The area of each individual feature
Major and minor axis lengths of feature	[mm]	Measurements of the longest and shortest dimensions of each feature
Total area of sample	[m^2]	The total analysed area of the sample
Total area of feature category	[mm^2]	The cumulative area covered by all features in a category
Derived metrics		
Aspect ratio (AR) of feature	[–]	$=\frac{majoraxislenghtoffeature}{minoraxislenghtoffeature}$
Density of feature category	[–]	$=\frac{totalnumberoffeatures}{totalareaofthesample}$
Normalised area of feature category	[–]	$=\frac{totalareaofafeaturecategory}{totalareaofthesample}$

In this context, a feature is defined as a single closed white contour in a binary image, while a feature category is the collection of features assigned to one of three classes: pores, vegetal material, and inorganic material.

The pipeline for step 6 is documented and available in the repository at https://doi.org/10.5281/zenodo.18007632.

Steps 7 and 8 – Multivariate Statistical Analysis and Classification: to explore correlations among morphological features and identify sample clustering patterns, multivariate statistical analysis was performed using custom Python scripts within PyCharm (JetBrains IDE, PyCharm, 2024).

Classical Principal Component Analysis (CPCA): initial dimensionality reduction was performed using CPCA based on the covariance matrix, which is appropriate for variables that differ substantially in magnitude or units. Singular value decomposition (SVD) was performed to extract three principal components. The proportion of variance explained by each component was calculated, and component loadings were scaled by the square root of their corresponding eigenvalues to generate interpretable biplots. These visualisations enabled identification of morphological patterns and sample clustering based on feature distributions across the bitumen-based composite samples.

However, CPCA exhibits high sensitivity to outliers: anomalous observations can disproportionately influence the first principal components, potentially obscuring the underlying structure of the regular data. This sensitivity compromises the reliability of dimensionality reduction in the presence of atypical observations (Hubert et al., 2005). Therefore, to address outlier sensitivity, Robust PCA was applied to obtain principal components less affected by atypical observations.

Robust Principal Component Analysis (RPCA): dimensionality reduction was performed on the filtered dataset obtained through a robust approach, enabling more reliable identification of intrinsic morphological patterns within the bitumen-based composite materials while minimising the influence of anomalous features. The regularisation hyperparameter λ was set to $1/\sqrt{(\max(m, n))}$, where m is the number of samples and n the number of variables. This formulation balances the trade-off between low-rank matrix approximation and sparse outlier separation.

Pairwise Pearson Correlation: pairwise correlations among features and samples, including normalised area and density of pores, vegetal and inorganic materials, were assessed using Pearson's correlation coefficient (r), which quantifies the strength and direction of linear relationships between continuous variables. Values range from –1 (perfect negative correlation) to +1 (perfect positive correlation), with

0 indicating no linear relationship.

4. Results

The image analysis of 59 bitumen-based composite samples revealed distinct compositional patterns across three primary feature categories: pores, vegetal and inorganic materials. The following sections present the morphological characterisation of these features and their distribution patterns, followed by multivariate statistical analysis to identify compositional clusters and assess their relationship with archaeological

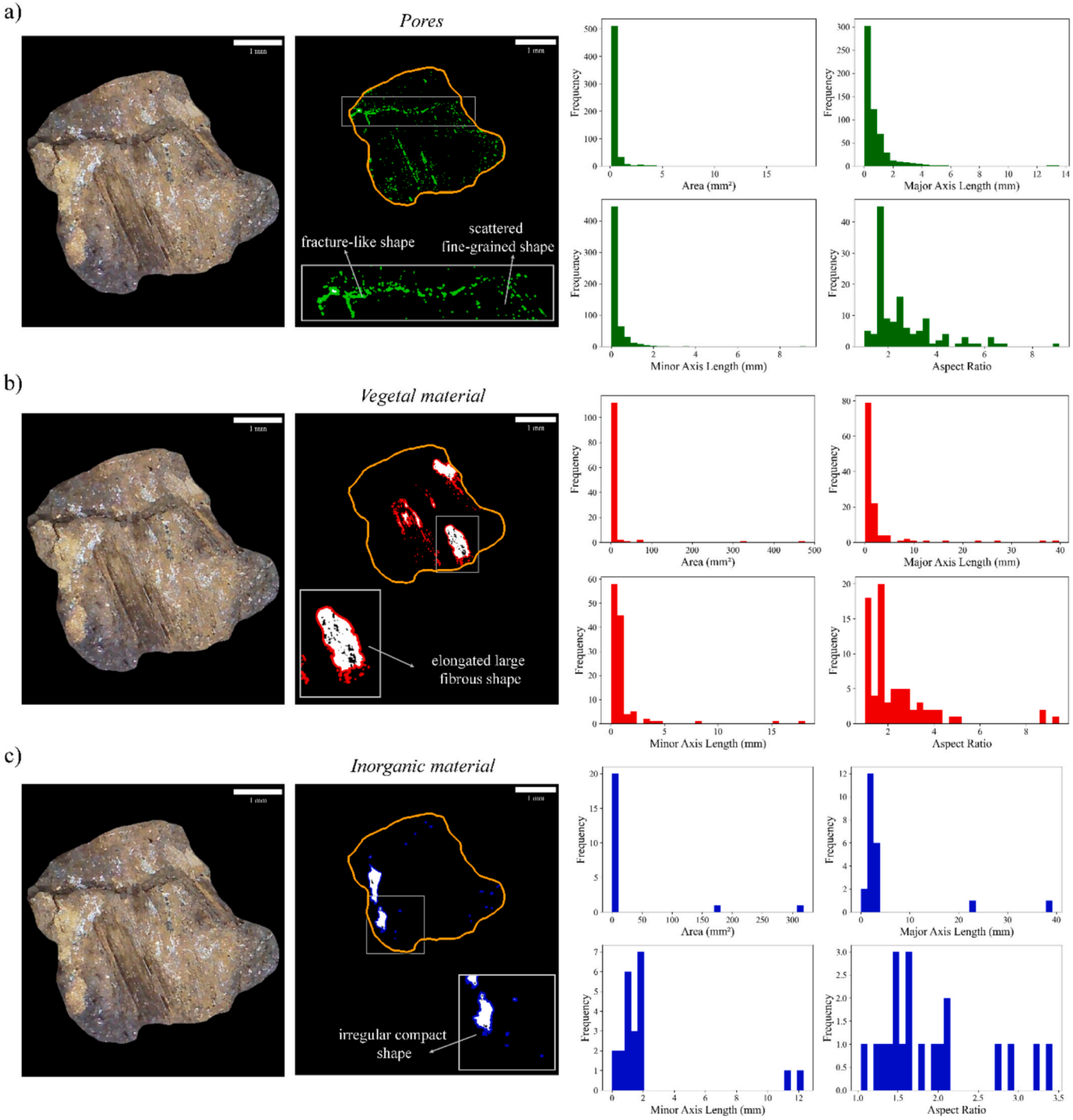

Fig. 4. Overlaid contours and histograms for Sample 27. Histograms show the frequency distribution of the four morphological parameters computed for each feature (see Table 2): major and minor axis lengths, area and aspect ratio (AR). a) Pores: detected pore contours overlaid in green. The grey magnified inset highlights the variety of pore morphologies observed in the analysed samples, ranging from large fracture-like voids to scattered fine-grained structures; b) Vegetal material: detected vegetal contours overlaid in red. The grey magnified inset displays the elongated, fibrous morphology that characterises most vegetal inclusions identified across the samples; c) Inorganic material: detected inorganic contours overlaid in blue. The magnified inset shows the variability in feature size despite their similarly compact and regular structure. In all cases, the overlaid contours enable qualitative assessment of segmentation accuracy. Sample contour is orange. The leftmost images in each panel correspond to the original microscopic photographs, upon which the detection contours have been overlaid. For all other samples, refer to the Supplementary Figs. S13–S48.

sample typologies.

4.1. Shape-based characterisation of feature categories (pores, vegetal, and inorganic materials)

Pores, vegetal, and inorganic materials display highly diverse morphologies, which were quantified using multiple shape descriptors. Fig. 4 illustrates the contrasting shapes and sizes among the three feature types through overlaid contours and histograms for a representative example (sample 27).

Pores are abundant, fine-grained, and widely distributed, appearing as very small, rounded, scattered voids with nearly circular shapes. Some pores exhibit fracture-like networks with irregular borders and orientations, while others form interconnected voids. Despite their abundance, pores occupy a minimal portion of the sample area, collectively representing a small proportion of the composite and have a limited influence on the overall mesostructure. While pores are ubiquitously present in all samples, the distribution of vegetal and inorganic materials is less frequent and more variable across the dataset.

Vegetal material, absent in samples 19, 21, 32, 33, 59, and 67, occurs mostly as large, elongated, well-defined fibrous structures (Fig. 4b), consistent with plant fibres or vegetal binders. However, some fragmented debris exhibit small, rounded shapes. Pores are also present within these vegetal structures. When present, vegetal features are significantly larger than pores, occupying a greater proportion of the image area and contributing substantially to the structural framework of the composites.

Inorganic material, not detected in samples 7, 13, 24, 42, and 59, was found in similar abundance to vegetal material but displayed highly variable structures, occurring either as large agglomerates or as small-grained particles with compact morphology and no internal porosity.

A summary of morphometric parameters obtained through image analysis of bitumen-based samples is provided in Supplementary Table S2.

The correlation matrix (Fig. 5a), based on pairwise Pearson correlation coefficients, revealed no correlation between the distribution and spatial extent of the three feature types detected in the sample images, either among or within features themselves. Pores and inorganic materials exhibited negligible correlation ($r < 0.30$) between normalised area and density, indicating highly variable proportions of sample surface area and inconsistent morphologies. In contrast, vegetal materials showed a positive correlation ($r > 0.80$) between these metrics, demonstrating high morphological homogeneity, as plant debris maintains relatively consistent sizes and shapes across samples.

4.2. Cluster identification and analysis of bitumen-based composites

To investigate compositional variability among the analysed samples, in terms of distribution and quantity of pores, vegetal and inorganic materials, multivariate statistical analyses were performed to identify underlying patterns and assess potential relationships with archaeological typologies.

Both Classical Principal Component Analysis (CPCA) and Robust Principal Component Analysis (RPCA) were conducted on a dataset of 59 samples × 6 variables: density and normalised area of pores, vegetal materials, and inorganic materials. In Fig. 6, samples are colour-coded according to typology (red = residues and traces, blue = spherical objects, grey = unidentified fragments, and green = ingots). Comparison between these complementary approaches allows assessment of outlier influence on variance structure and reveals whether extreme observations mask fundamental compositional patterns within the assemblage.

CPCA explained 99.62% of cumulative variance across three principal components (PC1: 57.95%, PC2: 32.99%, PC3: 8.68%). As shown in Fig. 6a, samples 44, 65, and 51 form a distinct cluster in the first quadrant of the biplot, characterised by high vegetal material normalised area along PC1. Additional samples (18, 40, 36, 34, and 23) also

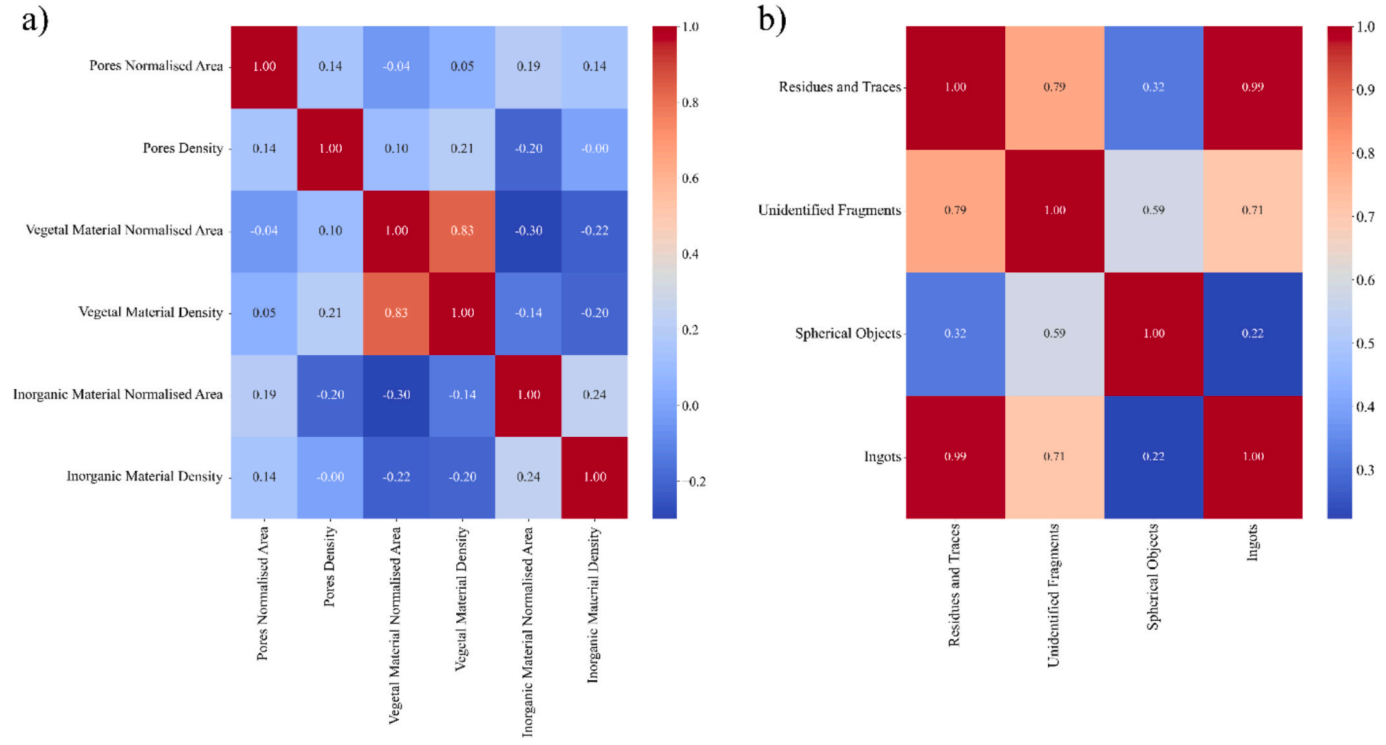

Fig. 5. Pairwise Pearson correlation matrices. a) Intra-sample correlation matrix showing relationships among normalised area and density measurements for the three feature types (pores, vegetal material, and inorganic material) across all samples. b) Inter-group correlation matrix based on mean vectors of normalised area and density for pores, vegetal material, and inorganic material within each functional typology. Colour scale represents correlation strength ranging from −1 (blue, negative correlation) to + 1 (red, strong positive correlation).

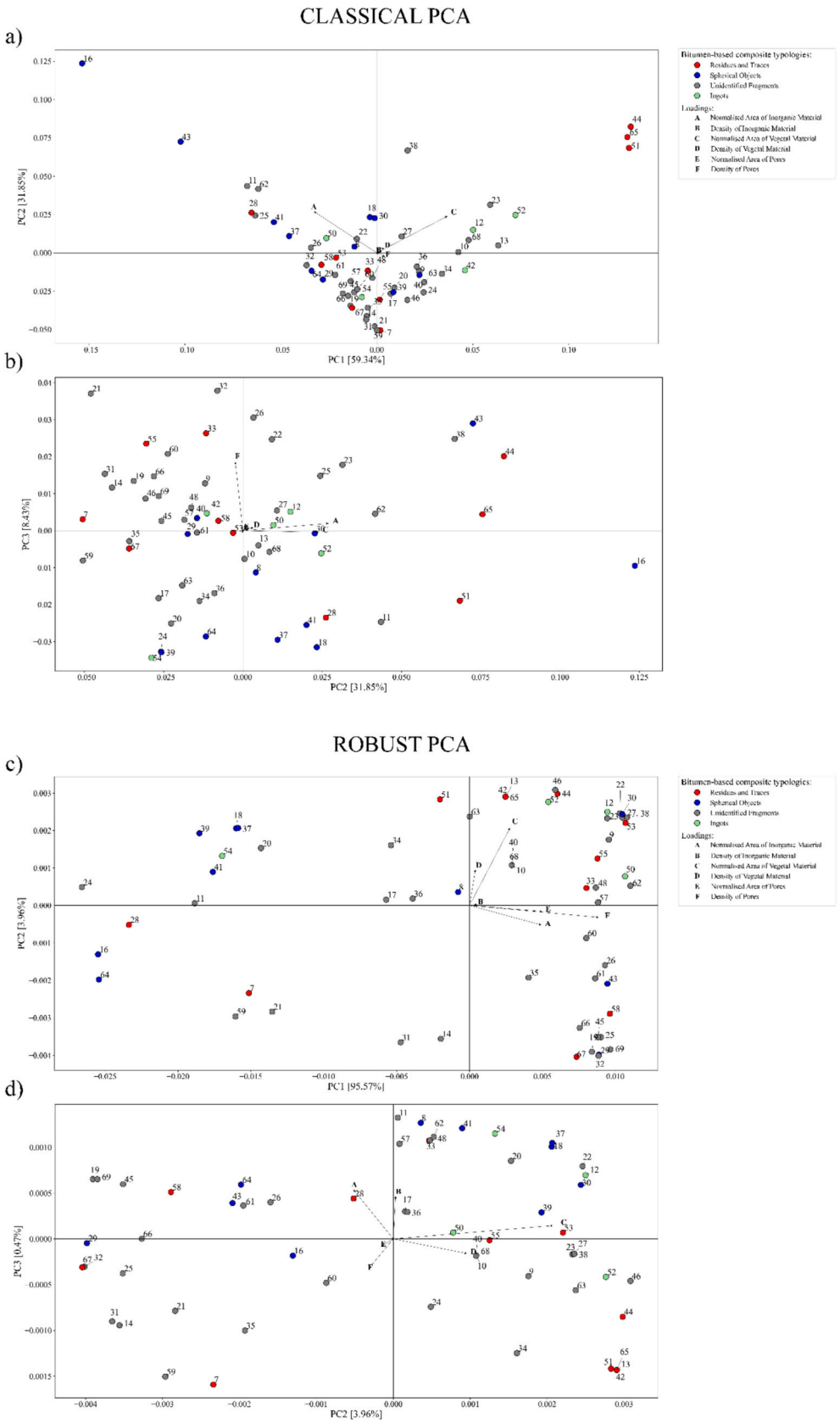

(caption on next page)

Fig. 6. Classical Principal Component Analysis (CPCA) biplots and Robust Principal Component Analysis (RPCA) biplots of the complete dataset 59 samples × 6 morphometric variables, including density and normalised area of pores, vegetal and inorganic materials. Arrows represent variable loadings indicating the direction and magnitude of each variable's contribution to the principal components. Sample scores are colour-coded by functional typology (as reported in the legend). For CPCA: a) PC1 vs. PC2, representing the primary variation within the assemblage; b) PC2 vs. PC3, capturing secondary patterns of compositional differentiation. The percentage of variance explained by each component is shown on the corresponding axis. For RPCA: c) PC1 vs. PC2, capturing the primary axes of variation; d) PC2 vs. PC3, revealing secondary patterns of sample differentiation. The percentage of variance explained by each component is indicated on the corresponding axis.

exhibit high amounts of vegetal content but occupy distinct quadrants, suggesting extreme values substantially impacted the PCA structure.

Samples 16 and 43, located in the second quadrant, are significantly separated from the vegetal-rich group, correlating with high inorganic material normalised area along PC2. Most samples cluster near the origin, forming a relatively homogeneous group in the third quadrant. Fig. 6b shows broader spread along PC2 and PC3, with pore density contributing primarily to PC3, particularly for samples 21 and 32. However, the strong signal of outliers raises the question of whether this variance structure shows genuine compositional importance or masks a more fundamental microstructural pattern characteristic of the assemblage. This observation motivated the application of a robust approach to re-evaluate the variance structure without disproportionate influence of extreme observations. RPCA downweights outlier influence to reveal clearer underlying structure through iterative reweighting. This approach yielded 99.99% cumulative variance (PC1: 95.57%, PC2: 3.96%, PC3: 0.47%), producing a less compact central grouping with improved cluster separation (Fig. 6c). Critically, it revealed a fundamentally different compositional variance structure: While CPCA was dominated by vegetal and inorganic content variation driven by outlier samples, RPCA identified pore density as the primary source of variation across the assemblage. Vegetal material normalised area now

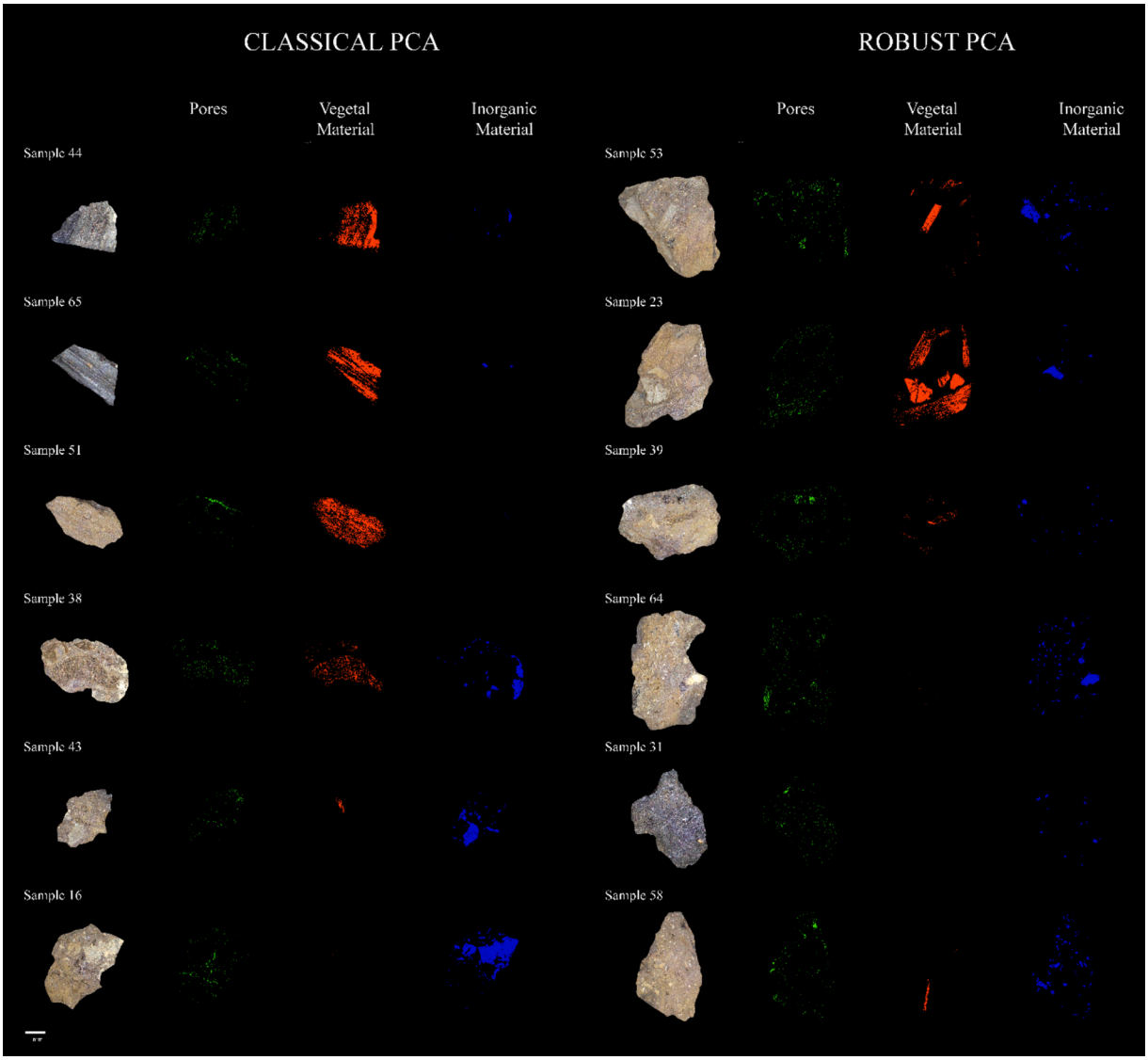

Fig. 7. Representative bitumen-based composite samples illustrating the main compositional variability along the PC1 and PC2 axes in Classical PCA (CPCA) vs Robust PCA (RPCA). In CPCA, samples 44, 65, and 51 exhibit the highest vegetal material content, while samples 16 and 43 are dominated by inorganic material. Sample 38 represents an intermediate composition with balanced vegetal and inorganic components. In RPCA all samples exhibit elevated porosity. Samples 53 and 23 are characterised by abundant vegetal material, whereas samples 64, 31 and 58, display minimal or absent vegetal content but high inorganic material. The comparison demonstrates how outlier removal in RPCA shifts the compositional space, emphasising porosity as a discriminating factor and revealing distinct patterns in material distribution.

contributes predominantly to PC2, while inorganic material normalised area is associated with PC3. This indicates that pore-related structure represents the dominant compositional variance once outlier influence is minimised.

Despite this variance redistribution, key compositional groups remained well-separated, validating them as genuine material categories rather than statistical artefacts. Importantly, the main variation captured by CPCA along PC1 and PC2 (vegetal and inorganic material normalised areas, respectively) was preserved in RPCA, manifesting as PC2 and PC3. Samples previously positioned as extreme outliers in CPCA (e.g. 41, 65, and 44) shifted closer to the main data cloud in RPCA, confirming that their extreme positions were artefacts of outlier sensitivity rather than indicators of true compositional distinctiveness. Nevertheless, these samples retained their relative positions along the principal component that best describes their specific compositional characteristics, demonstrating the robustness of the underlying patterns.

In CPCA, large vegetal structures in outlier samples capture disproportionate variance, overshadowing subtle but pervasive pore density variation that characterises most samples. RPCA reveals that mesostructural porosity variation constitutes the primary differentiation axis across the assemblage. While vegetal and inorganic materials create visually dramatic compositional differences in a subset of samples, pore-related features represent the fundamental variation shared across the entire dataset. This analysis confirms the choice between CPCA and RPCA addresses different research questions: CPCA identifies compositional extremes and exceptional samples, whereas RPCA characterises the dominant patterns within the bulk assemblage.

Fig. 7 shows representative samples that best correspond to the PCA plot distributions. For CPCA, the outlier samples 44, 65, and 51 contain numerous large and elongated vegetal structures occupying substantial surface area (first quadrant of Fig. 6a). Samples 16 and 43 display minimal vegetal material but contain high inorganic material (second quadrant of Fig. 6a), while sample 38 shows intermediate proportions. For RPCA, all samples display numerous small, uniformly rounded pores. Samples 53 and 23 (first quadrant of Fig. 6c) additionally exhibit abundant vegetal structures with low inorganic content. Inorganic material is high in samples 64, 31 and 58 (third and fourth quadrants of Fig. 6c) while sample 39 exhibits intermediate composition. This visual mesostructural evidence reconciles the apparent discrepancy between methods.

Examining typological distribution in the RPCA biplot reveals that compositional variation exists within functional typologies, though certain types exhibit greater internal consistency than others.

Bitumen-based residues and traces (red) show a relatively consistent pattern, with most samples (42, 44, 53, 55, 33, and 51) clustering in or near the first quadrant of the PC1/PC2 biplot (Fig. 6c; high pore density, elevated vegetal content). Exceptions include sample 28 (high vegetal, negligible porosity), samples 67 and 58 (high porosity, minimal or absent vegetal material), and sample 7 (moderate-to-low values for both features). In the PC2/PC3 biplot (Fig. 6d), this typological class displays variable degrees of inorganic content, although the majority show moderate-to-low content, predominantly located in the third and fourth quadrants.

Ingots (green) similarly favour the first quadrant of the PC1/PC2 biplot (Fig. 6c; samples 12, 50, and 52), though sample 54 diverges with abundant vegetal material but low pore density. Ingots generally have high inorganic material content, except for sample 52, located in the fourth quadrant of the PC2/PC3 biplot (Fig. 6d).

Spherical objects (blue) display the greatest heterogeneity across quadrants, despite forming local sub-clusters. In the PC1/PC2 biplot (Fig. 6c), samples 18, 39, and 41 group in the third quadrant (moderate vegetal content, low pore density). Samples 16 and 64 exhibit low values for both features, while sample 43 shows an opposing profile (high pores, negligible vegetal). Sample 30 combines high values of both features, and sample 8 has an intermediate composition. In the PC2/PC3 biplot (Fig. 6d), the majority of spherical objects are characterised by high levels of inorganic material, located in the medium-to-high range of PC3.

Unidentified fragments (grey) are widely scattered throughout the RPCA biplot spaces, although some specimens exhibit compositional affinities with multiple functional typological categories. In the PC1/PC2 biplot (Fig. 6c) first quadrant associations include: samples 48 and 57 with residue/trace sample 33; sample 62 with ingot sample 50; and samples 23, 22, and 38 with ingot, spherical object, residue/trace samples 12, 30, and 53 respectively. Second quadrant clustering places samples 20 and 11 near spherical objects 41 and 37. Third quadrant positioning shows samples 59 and 21 proximate to residue and trace sample 7. The fourth quadrant contains a large unidentified group—samples 66, 45, 19, 25, 32, 69, and 29—clustering near ingot samples 67 and 58, and samples 61 and 26 positioned near spherical object sample 63. In the PC2/PC3 biplot (Fig. 6d), the inorganic content is extremely variable in these samples, scattered throughout the entire plot space.

To evaluate similarities and differences across sample typologies, a Pearson correlation matrix was computed. The correlation matrix (Fig. 5b), calculated from mean vectors of the 6 variables used for PCA, reveals patterns among sample typologies: (i) residuesand traces and ingots exhibit the strongest inter-group affinity ($r > 0.90$), suggesting shared compositional and mesostructural characteristics. (ii) Spherical objects occupy a distinct position within the multivariate space, displaying weak to negligible correlation with other groups ($r < 0.32$). (iii) Unidentified fragments manifest intermediate correlation behaviour, maintaining strong positive associations with both residues and traces ($r \approx 0.80$) and ingots ($r \approx 0.70$), while exhibiting only moderate correlation with spherical objects ($r \approx 0.60$).

Within-typology correlation analysis reveals that vegetal-related metrics dominate the covariance structure. Specifically, normalised area and density are positively correlated ($r > 0.95$) in three of four investigated sample typologies, demonstrating a proportional scaling between the spatial distribution and concentration of vegetal materials. A notable exception occurs within ingots, where a positive relationship is observed between the normalised area of pores and inorganic material ($r > 0.6$).

5. Discussion

5.1. Compositional variability and functional interpretation across sample typologies

This section discusses the compositional variability of sample typologies, focusing on differences and similarities in porosity, vegetal, and inorganic materials.

All samples exhibit an inherently porous structure, with pores ubiquitously present across all typologies. Porosity represents a universal characteristic, potentially intrinsic to material processing techniques. Some pores form agglomerated, fracture-like networks that may reflect mechanical stresses during archaeological deposition, mixing processes during intentional manufacture (Jing et al., 2023), or post-depositional effects such as deterioration of vegetal debris or leaching of inorganic components.

In contrast, vegetal and inorganic materials vary considerably between samples. While some samples contain minimal or no vegetal and inorganic materials, others show substantial amounts that contribute significantly to the visual and spatial mesostructure. No spatial correlation was detected among the three features (pores, vegetal, and inorganic materials), indicating independent formation processes. Only vegetal material shows positive correlation between normalised area and density, as plant debris maintains relatively consistent sizes and shapes across samples. Inorganic material displays highly variable morphology, occurring as large agglomerates or fine-grained particles, but generally maintains a compact structure with no internal porosity.

Despite these diverse morphologies—including varying colours

(white, grey, yellow–brown)—no significant differences were observed at the spectroscopic scale. X-ray Fluorescence (XRF) analysis, presented in detail in an ongoing publication, revealed four distinct elemental fingerprints that characterise the samples:

(1) calcium (Ca) enrichment with associated strontium (Sr), and absence of other elements, indicating carbonate dominance (Fig. 8a). Ca shows high concentrations, attributed to calcite occurring as primary carbonate, secondary precipitates, and reworked material, with likely contributions from biogenic sources (shell fragments). Sr consistently correlates with Ca, characteristic of biogenic and marine-influenced carbonates where Sr^{2+} substitutes for Ca^{2+} in carbonate lattices.
(2) elevated sulphur (S) and chlorine (Cl) levels (Fig. 8b). S concentrations are consistently elevated and frequently exceed iron, indicating that sulphate minerals (gypsum/anhydrite) constitute the dominant S-bearing phases rather than pyrite. Cl is widely present, while sodium (Na) is nearly absent, excluding halite and suggesting that Cl is hosted in secondary salts or introduced by concentrated brackish fluids. The lack of Na–Cl coupling supports a post-depositional or fluid-mediated origin for Cl, consistent with diagenesis driven by concentrated fluids and evaporitic processes.
(3) silicon (Si)–potassium (K)–titanium (Ti)-iron (Fe) assemblage, marking siliciclastic input (Fig. 8c). Si displays moderate concentrations consistent with quartz and siliciclastic background, while K indicates phyllosilicate phases (illite, K-feldspars). Ti indicates detrital heavy minerals (ilmenite).
(4) iron and associated trace metals (titanium, chromium (Cr), manganese (Mn), nickel (Ni), and bromine (Br)) (Fig. 8d). Fe occurs at moderate concentrations primarily as oxides (hematite/goethite) and does not correlate with S, indicating spatially or temporally limited pyrite formation and predominantly oxidising diagenetic conditions.

This geochemical signature indicates repeated episodes of carbonate precipitation and sediment reworking in a restricted brackish-lagoonal environment, influenced by fluvial detrital input from the Tigris–Euphrates system, evaporitic sulphate formation, and saline fluid circulation. These data confirm the local provenance of inclusions within samples and demonstrate that during the Middle Holocene the area experienced brackish to marine conditions, transitioning to freshwater in the Late Holocene due to seaward progradation of the deltaic rivers.

Residues and Traces: these specimens on objects exhibit high mesostructural heterogeneity, despite being characterised by a dominant vegetal component. The inorganic material is absent or negligible, while porosity is highly irregular and variable, reflecting poor structural coherence. The variable distribution and morphologies of these features likely reflect distinct technological choices and functional requirements.

Bitumen-based adhesive: samples from flint sickle blades, samples 7, 44, and 55 (Fig. 2a), and sarcophagus repair (sample 51) (Fig. 2c) share elevated porosity and vegetal content with generally low inorganic material. Both hafting applications and structural bonding required flexible gap-filling compositions. The abundant vegetal content likely enhanced elasticity and crack resistance, while the low inorganic content prevented excessive shrinkage during curing.

Grindstone residue: sample 28 (Fig. 2e) is characterised by high inorganic content, low vegetal material, and limited porosity. This composition reflects mechanical processing of bitumen on the grindstone itself, where repeated grinding reduced the material to a compact, mineral-rich powder, possibly incorporating lithic particles from the grinding surface.

Bitumen applied to reed-based artefacts: samples 53 and 65 share elevated levels of porosity and vegetal material, indicating their fibrous substrates. Sample 53, collected from a reed mat placed between a sarcophagus rim and lid, contains high inorganic content, while sample 65 (Fig. 2d), associated with a reed-woven basket, shows considerably lower levels. The abundant vegetal content likely derived from fibre imprints, though vegetal-rich bitumen may have been prepared to reduce flowability and improve adhesion and flexibility for use as a coating or sealant. The elevated inorganic content in sample 53 may

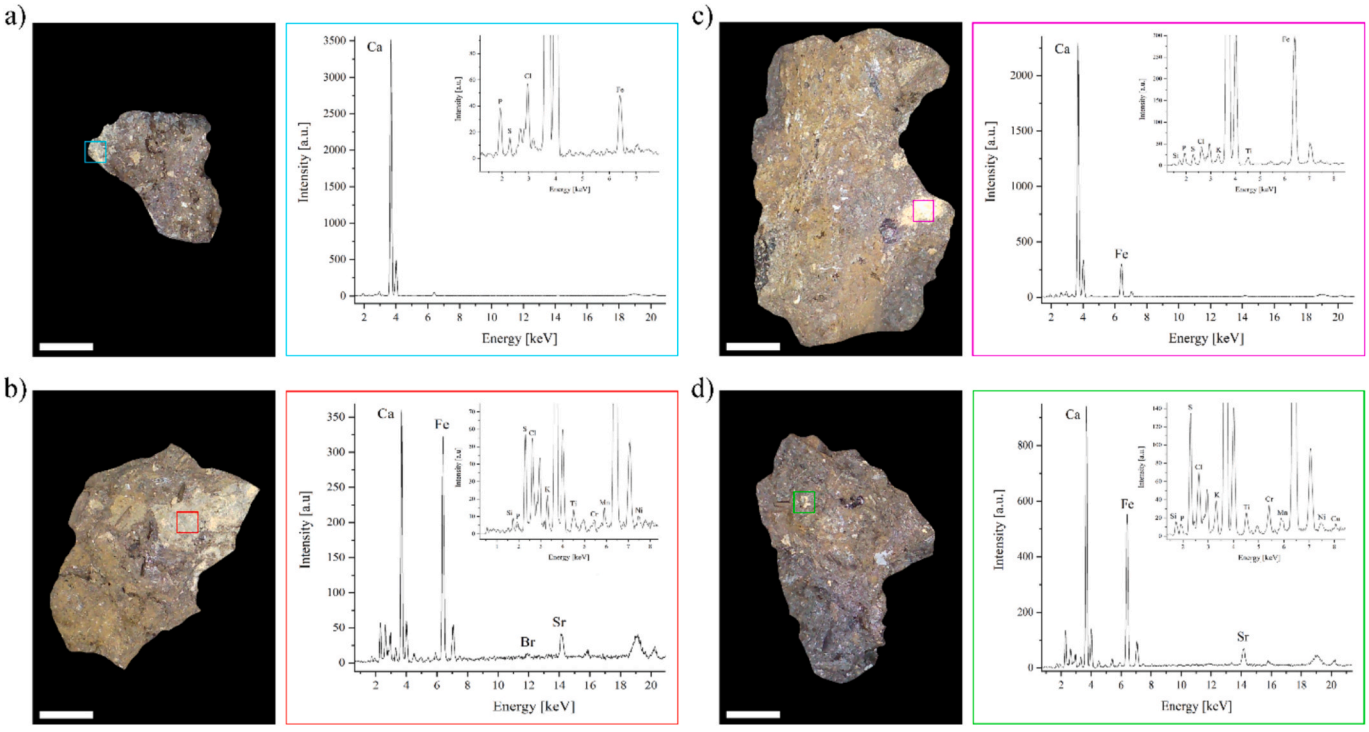

Fig. 8. XRF analysis of the samples revealed a similar elemental composition across all specimens. Four distinct elemental fingerprints were identified: a) Ca-rich composition; b) S-Cl-bearing phases; c) Si-K-Fe-Ti assemblage; d) Fe-Ti-Cr-Mn-Ni-Br association. Scale bar = 1 mm.

result from contact with the stone sarcophagus surface or environmental contamination. More broadly, these data suggest that reed mats and baskets were routinely waterproofed prior to use, with their eventual deposition in funerary contexts reflecting one of the possible uses.

Bitumen-based vessels and incrustations: sample 33 (Fig. 2f) consists of fragments with preserved rims and intentionally shaped concave surfaces, indicating manufacture as small vessels made entirely from bitumen. Sample 67 represents an interior incrustation from a medium-to-large ceramic jar whose inner surface was heavily coated with bitumen. Sample 58, a flat bitumen-based fragment found among several other fragments presumably stored for re-melting, has an ambiguous interpretation rather than a clearly defined object type: it may have been either part of a complete bitumen-based vessel or an incrustation removed from a ceramic container.

All three samples show high porosity and substantial inorganic content but differ markedly in vegetal material: sample 33 contains high levels, while samples 58 and 67 show considerably lower amounts. The close compositional similarity between samples 58 and 67, particularly in their low vegetal content, more plausibly supports an interpretation of sample 58 as an incrustation rather than as a vessel fragment, suggesting shared functional requirements or production contexts. The minimal vegetal content indicates a storage and sealing function—the ceramic vessel from which sample 67 derives likely stored bitumen or served as a container for waterproofing agents—contrasting with sample 33, where high vegetal content enhanced structural integrity and workability during vessel manufacture.

This typological class demonstrates a broad spatial distribution across Buildings A, D, and E, with a marked concentration in domestic contexts that points to their integration into daily household practices. Residues and traces represent a final discard phase associated with site abandonment, when functional objects were no longer serviceable or necessary.

Two samples (51, 53) deviate from this pattern: despite their recovery from a burial context, these artefacts show clear evidence of utilitarian function rather than being connected to ritual practices linked to funerary deposition. Their use in repair, covering, and waterproofing activities suggests a clear pragmatic use.

Sample 58 represents a partial exception: although it was recovered from a burial context, the burial pit cuts through the workshop area, making it likely that the fragment originated from workshop-related deposits and was redeposited within the grave fill during excavation and backfilling. Its presence in the burial context therefore reflects secondary deposition rather than intentional funerary use.

Sample 55 stands apart as the only artefact of its kind from the workshop area. It consists of a sickle with bitumen-based adhesive, likely related to hafting or re-hafting activities, possibly including the rotation and re-setting of blades. The presence of lithic blades showing bilateral retouch and evidence of heat exposure supports this interpretation. A detailed discussion of this artefact is presented elsewhere (D'Errico 2019; Moscone 2019; Manclossi and Romano 2024).

Ingots: samples 12, 42, 54, and 52 exhibit a systematic presence of vegetal and inorganic materials and relatively stable porosity, indicating minimal internal variability. Sample 52 has lower amounts of inorganic materials, while sample 54 (Fig. 2b) exhibits lower porosity. This consistency suggests standardised production methods that may have involved preliminary processing steps, including heating and softening natural bitumen, the addition of vegetal and inorganic materials, and shaping into standardised forms for storage and distribution. Such practices would be consistent with the production of ready-to-use bitumen-based materials (Connan et al., 2023) suitable for immediate application, potentially reflecting specialised production centres and standardised recipes tailored for particular applications. The abundant vegetal fibres observed in the samples may also derive from protective reed mat wrappings, with fibres transferring to the bitumen through contact. The ingots are characterised by clear pattern impressions consistent with reed mats commonly documented in domestic contexts. These impressions suggest that the ingots were at least partially wrapped or placed on reed mats, likely to facilitate handling and stacking, with the mat covering the flat surface and extending over the shorter sides.

Spherical Objects: samples 64, 43, 16, 8, 30, 37, 18, 39, 41, 29, and 40 form a clearly distinct group when compared to the other classes, showing a highly consistent and coherent microstructural signature. Their porosity is remarkably stable, and the inorganic material is systematically present at moderate-to-high levels of area coverage but low densities. This combination suggests the presence of fewer but larger or more coherent inorganic inclusions, consistent with intentional aggregation or shaping processes. In contrast, other classes often show either negligible inorganic content or highly variable distributions. Vegetal material plays a minor and non-structural role, particularly low in samples 64, 43, 16, and 29 (Fig. 2g), supporting the interpretation that vegetal material is incidental rather than functionally relevant in the formation of spherical objects. These features collectively indicate intentional manufacture and controlled formation processes. The spherical objects are unlikely to represent standardised pre-products, as their compositional variability (Festa et al. 2025) suggests that they do not share a uniform recipe. Rather, they may represent intermediate forms produced during bitumen handling and processing. Several spherical objects were recovered from a pit associated with Phase 2 of Room 23, indicating their deliberate accumulation and storage. These spheres may have been formed opportunistically when excess molten bitumen remained after processing activities, shaped into manageable units for later reuse, a practice observed also at the Hit oil seeps (Connan, 1997).

The variability in vegetal content supports this interpretation, suggesting that vegetal additives were not systematically incorporated at this stage but were more likely added later, during subsequent melting and preparation for specific applications. The ubiquitous inorganic component may derive either from the geological source or from incidental incorporation during handling and shaping. Overall, the spherical form appears to reflect a practical solution for storing and managing bitumen in intermediate stages of the operational sequence, rather than the production of standardised end products.

Significantly, both ingots and spherical objects were recovered from household contexts, supporting their identification as intermediate products stored on-site for immediate or future use. This pattern indicates household-level bitumen processing, with families or craft specialists maintaining stocks of semi-processed material for final preparation according to specific task requirements—a decentralised model contrasting with centralised production systems and reflecting distributed technological knowledge across the community.

Unidentified Fragments: these specimens (Fig. 2h) display the highest internal variability among all classes. Their compositional overlap with multiple recognised typologies suggests analogous production processes, shared functional roles, or that some fragments represent degraded examples of identified typological categories. This lack of coherence suggests that these samples do not represent a single functional or technological category, but rather a mixed assemblage of broken, altered, or incompletely formed materials. Their microstructural diversity likely reflects multiple formation pathways, including mechanical fragmentation and post-depositional alteration. Assigning these fragments to a specific functional class is not possible based solely on image analysis.

In Festa et al. (2025), the classification of unidentified fragments into distinct archaeological typologies was achieved using a Support Vector Machine (SVM), trained exclusively on FTIR spectroscopic data from labelled samples. This supervised machine learning analysis revealed that several unidentified fragments (e.g., 10, 14, 25, 36, 63, and 68) resemble ingots, others (9, and 11) are similar to adhesives, some (19, 24, 38, 59, and 62) correspond to bitumen-based vessels and incrustations, while the majority (13, 20, 21, 22, 23, 27, 31, 32, 34, 53, 57, 66, and 69) are comparable to spherical objects.

Among these classes, differences were observed in the preservation

of the hydrocarbons characteristic of the bitumen matrix, namely the saturated aliphatic bands (2952 cm^{-1} – ν_asym CH_3; 2920 cm^{-1} – ν_asym CH_2; 2850 cm^{-1} – ν_sym CH_2; 1380 cm^{-1} – δ CH_3; 720 cm^{-1} – rocking CH_2) and the aromatic bands of asphaltenes (1600 cm^{-1} – ν C═C and ν C–H aromatic; 1640 cm^{-1} – conjugated ring vibrations). Additional chemical signals were detected, showing ageing processes (3300–3400 cm^{-1} – hydroxyl groups from oxidation; 1700 cm^{-1} – carbonyl groups; 1030 cm^{-1} – sulphoxide groups), environmental contamination, or the deliberate addition of mineral fillers. These include carbonates such as calcite and aragonite (875 cm^{-1} – δ CO_3^{2-}; 1400–1500 cm^{-1} – ν CO_3^{2-}), silicates including quartz, feldspars, and clays (1057 cm^{-1} – ν Si–O), and sulphones as oxidative products (1310 cm^{-1}, 1160 cm^{-1}).

Residues, traces, and ingots share a relatively pure and homogeneous chemical profile, with limited evidence of added materials. This pattern may reflect an early stage in the operational sequence, consistent with textual sources describing bitumen arriving at the sites either as solid blocks or in liquid form, prior to further modification or mixing. While this interpretation remains tentative, it is compatible with the compositional simplicity observed in these categories.

Spherical objects display a heterogeneous chemical composition: the hydrocarbon bands are less intense, and the bitumen matrix appears mixed with carbonates and silicates, indicative of either environmental contamination or intentional mineral fillers.

Bitumen-based vessels and incrustations represent the most degraded samples, where the characteristic CH bands are absent or significantly reduced. The bitumen matrix also exhibits high levels of contaminants—possibly reflecting waste products set aside for recycling.

These FTIR spectroscopic data are consistent with and confirm the distinctions identified through the mesoscopic analysis presented in this work, providing complementary chemical evidence for the morphological differences observed among artefact categories.

5.2. Ancient and modern bitumen technology: a comparative perspective

The comparison between Sumerian bitumen processing techniques and modern methods reveals remarkable continuities in material engineering principles, particularly in the strategic use of additives to tailor material properties for specific applications. This technological persistence across millennia reflects the inherent validity of these engineering solutions to universal material challenges.

Our functional analysis demonstrates that ancient Mesopotamian craftsmen developed distinct bitumen formulations, each optimised for particular applications. Bitumen-based composites containing vegetal material with minimal inorganic content functioned as adhesives, maintaining sufficient viscosity for bonding while avoiding excessive hardness (Connan et al., 2013). The plant fibres provided crucial viscoelastic properties, enabling the adhesive to absorb mechanical stresses and withstand thermal cycling without losing cohesion.

For applications requiring penetrative or lubricant properties, Sumerian artisans produced pure liquid bitumen through controlled thermal processing—either through unidirectional heating (Schwartz & Hollander, 2000) or by decanting the fluid phase from heated containers. This low-viscosity product proved ideal for specialised applications where mineral inclusions would compromise outcomes: decorative work, statue affixing, and pottery repair—all of which demanded this pure form to maintain both aesthetic quality and structural integrity (Daneels et al., 2018). This distinction between liquid and solid bitumen formulations seems to be corroborated by cuneiform sources, which apparently document intentionally differentiated compositions adapted to specific functional and logistical needs—solid forms might have circulated as ingots, while liquid bitumen was possibly transported in jars, each following distinct preparatory recipes (Stol 2012).

Formulations that combined both vegetal and inorganic materials in balanced proportions, were used for sealants and waterproofing agents. Inorganic additives contributed mechanical strength and durability, while vegetal materials enhanced adhesion, flexibility, and crack resistance. However, excessive inorganic content would induce brittleness, necessitating vegetal additives to restore balance (Connan et al., 2023). This deliberate calibration demonstrates an empirically sophisticated understanding of composite material behaviour, achieved through iterative experimentation across generations.

Economic factors profoundly shaped bitumen formulation strategies. As a valuable commodity travelling considerable distances from geological sources, bitumen represented a costly material for ancient communities. This scarcity drove multiple adaptive strategies that reveal sophisticated resource management practices remarkably parallel to modern sustainability concerns.

Diluting bitumen with mineral and plant debris served as a pragmatic approach to extending limited supplies while maintaining acceptable performance. The resulting mixture increased in volume, effectively 'stretching' available supplies—a strategy that balanced economic constraints with technical needs (Schwartz & Hollander, 2000). Moreover, vegetal-rich samples indicate systematic recycling practices. Recovered bitumen underwent reprocessing through heating, often with added vegetal material to lower melting points and facilitate reuse. Direct archaeological evidence from Oman documents populations systematically collecting bitumen-based mixtures from reed boats for reprocessing (Connan et al., 2023), confirming that ancient societies developed sophisticated practices for conserving and repurposing valuable materials.

While pure natural bitumen possesses favourable characteristics—viscosity, adhesiveness, and water repellence—it also presents inherent limitations: excessive stickiness in dynamic applications, low thermal resistance causing problematic softening in hot climates, and polymerisation upon air exposure leading to progressive hardening. Ancient craftsmen, like modern engineers, addressed these limitations through carefully formulated additions of vegetal and inorganic materials. This continuity in bitumen technology confirms that fundamental recipes have persisted from the Neolithic to today (Connan, 1997), though modern practice has rationalised and optimised these formulations, decreasing the amount of bitumen required while maintaining or enhancing performance.

Modern asphalt technology provides compelling validation of ancient practices. Incorporating vegetal fibres and inorganic additives at levels between 0.1% and 0.5% by total mixture weight demonstrably enhances bitumen performance (Mashaan et al., 2021; Aitkaliyeva et al., 2023). Vegetal fibres—including silk, cotton, jute, coconut, and hemp—improve cohesion between aggregates and binder, increasing fatigue resistance, durability, and low-temperature crack control while reducing bleeding. Inorganic additives—such as limestone, silica, fly ash, zeolites, and nanoclays—reduce ageing effects by slowing oxidation, regulate viscosity, and maintain structural integrity.

6. Conclusion

The mesostructural analysis of compositional variability in ancient Sumerian bitumen-based artefacts establishes that Mesopotamian craftspeople employed sophisticated material engineering principles that strikingly converge with modern asphalt technology. This study reveals a complex *chaîne opératoire* based on specialised formulations deliberately tailored to balance functional requirements with economic constraints. The significant variability in vegetal and inorganic materials across different artefact typologies indicates intentional technological choices rather than random processing. While a generally porous structure constitutes a universal intrinsic characteristic, the precise regulation of additive proportions was crucial for tailoring bitumen properties to specific end-use requirements.

Distinct compositional 'recipes' emerged corresponding to particular functional needs.

Adhesives for sickle blades and sarcophagus repairs required

flexibility and elasticity, achieved through high vegetal content and low inorganic material, which promoted gap-filling and crack resistance—demonstrating controlled bonding strength optimisation.

Sealants and coatings utilised balanced additive mixtures where inorganic material provided mechanical strength while vegetal content enhanced adhesion and flexibility, demonstrating optimised flow properties and enhanced durability through empirical understanding of composite material behaviour.

Ingots represented pre-formulated trade products characterised by systematic presence of vegetal and inorganic material, providing structural integrity and processability.

Spherical objects showed consistent and controlled microstructure with systematic inorganic content and minimal vegetal materials, suggesting intentional manufacture as units shaped to facilitate handling and storage.

The scarcity and high cost of bitumen as a commodity necessitated sophisticated resource management strategies. Diluting bitumen with mineral and plant debris represented a pragmatic approach to extending limited supplies while maintaining essential functional properties. Furthermore, the systematic presence of vegetal-rich samples points to widespread recycling practices, where material was deliberately reprocessed with added vegetal matter to restore workability—reflecting a circular economy approach to valuable resources.

The principles of material engineering observed in Sumerian practices—utilising vegetal fibres and inorganic fillers to control viscosity, enhance adhesiveness, and increase durability—are fundamentally validated by and persist in modern asphalt technology. Contemporary formulations similarly employ organic and inorganic modifiers to optimise performance characteristics, confirming a striking convergence that demonstrates advanced empirical understanding of polymer chemistry, mechanical properties, and processing parameters.

This technological endurance across millennia stands as compelling testimony to the ingenuity and scientific insight of ancient Mesopotamian craftsmen. Their empirical discoveries, developed through generations of systematic observation, controlled experimentation, and intergenerational knowledge transmission, anticipated fundamental principles that modern materials science would later codify through theoretical frameworks and quantitative analysis—demonstrating that technological sophistication need not depend on formal theory but emerges from deliberate practice addressing universal material challenges.

7. Software availability

The software used to process microscopic images and extract pore features, as described in this manuscript, is openly available via Zenodo.

The repository includes all scripts and parameters necessary to reproduce the analyses.

* Repository: Zenodo
* https://doi.org/10.5281/zenodo.18007818
* Version: Archived version available at the time of publication
* License: MIT License

The software used to process microscopic images and extract vegetal and inorganic material features, as described in this manuscript, is openly available via Zenodo.

The repository includes all scripts and parameters necessary to reproduce the analyses.

* Repository: Zenodo
* https://doi.org/10.5281/zenodo.18007711
* Version: Archived version available at the time of publication
* License: MIT License

The software used to process binary images with feature masks and compute morphometric parameters, as described in this manuscript, is openly available via Zenodo.

The repository includes all scripts and parameters necessary to reproduce the analyses.

* Repository: Zenodo
* https://doi.org/10.5281/zenodo.18007632
* Version: Archived version available at the time of publication
* License: MIT License

Acknowledgements

We thank the Italian Ministerial as founder of the PRIN 2021 grant. We also thanks reviewers for their thorough and thoughtful work, which significantly improved the quality of this paper. We also gratefully acknowledge our colleagues from the Iraqi State Board of Antiquities and Heritage for their support and for granting the necessary permissions for the export and analysis of the samples. The authors from CREF - Museo Storico della Fisica e Centro Studi e Ricerche “Enrico Fermi” would like to thank the institution for its support within the framework of the Physics for Cultural Heritage Research.

Ethics

No ethical issues are declared.

Founding sources

This research has been supported by the Italian Ministerial grant PRIN 2021 titled SLOW SUMER. Repair, Reuse, Recycling and Southern Mesopotamian Society in the Changing World of 2500–2000 BCE, Project Code 2022LKPNH, CUP MASTER – B53D23001740006.

Appendix A. Supplementary data

Supplementary data to this article can be found online at https://doi.org/10.1016/j.jasrep.2026.105607.

References

Aitkaliyeva, G., Yelubay, M., Vaičiukynienė, D., Ismailova, A., Amitova, A., Ibraimbayeva, G., 2023. Mineral additives based on industrial waste for modifications of Bitumen Polymers. Sace 32, 196–204. https://doi.org/10.5755/j01.sace.32.1.32505.

Boeda, E., Bonilauri, S., Connan, J., Jarvie, D., Mercier, N., Tobey, M., Valladas, H., Muhesen, S., 2008. Middle Palaeolithic bitumen use at Umm el Tlel around 70 000 BP. Antiquity 82 (318), 853–861. https://doi.org/10.1017/S0003598X00097623.

Breu, A., Alcántara, R., Arnaiz, R., Colomer, F., Moya, A., Sisa, J., 2017. Detection, recovery and analysis of visible bitumen residues in pottery from tell Lashkir, Kurdistan, Iraq. X Jornadas De Jóvenes En Investigación Arqueológica. 566–577.

Breu, A., Rosell-Melé, A., Molist, M., Bach-Gómez, A., 2022. Bayesian mixing models as a tool to explore Bronze Age bitumen trade from tell Lashkir (Erbil, Iraq). J. Archaeol. Sci. 145, 105643. https://doi.org/10.1016/j.jas.2022.105643.

Cârciumaru, M., Ion, R.-M., Niţu, E.-C., Ştefănescu, R., 2012. New evidence of adhesive as hafting material on Middle and Upper Palaeolithic artefacts from Gura Cheii-Râşnov Cave (Romania). J. Archaeol. Sci. 39, 1942–1950. https://doi.org/10.1016/j.jas.2012.02.016.

Cereda, S., 2019. Micro-debris analysis of Building A-Phase 1 Room 23. In: Romano, L., D'Agostino, F. (Eds.), Abu Tbeirah Excavations i. Area 1. Last Phase and Building A – Phase 1. Sapienza Università Editrice, Rome, pp. 311–320.

Connan, J., 1997. Le bitume dans l'antiquité. Bull. De L'A.MI.S 1–16.

Connan, J., Lombard, P., Killick, R., Højlund, F., Salles, J.-F., Khalaf, A., 1998. The archaeological bitumens of Bahrain from the Early Dilmun period (c.2200 BC) to the sixteenth century AD: a problem of source and trade. Arab. Archaeol. Epigr. 9, 142–481.

Connan, J., Oates, J., 2018. The bitumen of tell Brak from the Middle Uruk (c.3500 BC) to late Bronze Age (c.1280 BC): origin and trade routes. J. Hist. Archaeol. Anthropol. Sci. 3. https://doi.org/10.15406/jhaas.2018.03.00163.

Connan, J., Carter, R., Crawford, H., Tobey, M., Charrié-Duhaut, A., Jarvie, D., Albrecht, P., Norman, K., 2005. A comparative geochemical study of bituminous boat remains from H3, As-Sabiyah (Kuwait), and RJ-2, Ra's al-Jinz (Oman). Arab. Archaeol. Epigr. 16, 21–66. https://doi.org/10.1111/j.1600-0471.2005.00041.x.

Connan, J., Elezi, G., Engel, M.H., Zumberge, A., 2024. Natural asphalt on Late Neolithic (5000–4500 BCE) potsherds from southeastern Albania: a geochemical study. J. Archaeol. Sci. Rep. 53, 104343. https://doi.org/10.1016/j.jasrep.2023.104343.

Connan, J., Ghidoni, A., Mezzatesta, E., Joliot, C., Mathe, C., Vosmer, T., Gley, R., Bihannic, I., Pavan, A., Engel, M.H., Zumberge, A., 2023. Geochemical study of the luting and coating of medieval watercraft from the ship timbers discovered in the citadel of al-Balīd, Oman: Composition and origin. J. Archaeol. Sci. Rep. 49, 104051. https://doi.org/10.1016/j.jasrep.2023.104051.

Connan, J., Kavak, O., Akin, E., Yalçin, M.N., Imbus, K., Zumberge, J., 2006. Identification and origin of bitumen in Neolithic artefacts from Demirköy Höyük (8100 BC): Comparison with oil seeps and crude oils from southeastern Turkey. Org Geochem. 37, 1752–1767. https://doi.org/10.1016/j.orggeochem.2006.07.023.

Connan, J., Kavak, O., Sağlamtimur, H., Engel, M., Zumberge, A., Zumberge, J., 2018. A geochemical study of bitumen residues on ceramics excavated from Early Bronze age graves (3000–2900 BCE) at Başur Höyük in SE Turkey. Org Geochem. 115, 1–11. https://doi.org/10.1016/j.orggeochem.2017.09.007.

Connan, J., Kozbe, G., Kavak, O., Zumberge, J., Imbus, K., 2013. The bituminous mixtures of Kavuşan Höyük (SE Turkey) from the end of the 3rd millennium (2000BC) to the medieval period (AD 14th century): Composition and origin. Org Geochem. 54, 2–18. https://doi.org/10.1016/j.orggeochem.2012.09.007.

Connan, J., Zumberge, J., Imbus, K., Moghaddam, A., 2008. The bituminous mixtures of Tall-e Abu Chizan: a Vth millennium BC settlement in southwestern Iran. Org Geochem. 39, 1772–1789. https://doi.org/10.1016/j.orggeochem.2008.07.004.

Connan, J., Van de Velde, T., 2010. An overview of bitumen trade in the Near East from the Neolithic (c.8000 BC) to the early Islamic period. Arab. Arch. Epig. 21, 1–19.

Cosac, M., Murătoreanu, G., Radu, A., Ion, R., 2013. Arguments concerning the use of bitumen as adhesive for the hafting of some lithic tools from the Early Bronze Age in the region of the Curvature Subcarpathians. Ann. Univ. Valahia Târgovişte Sect. Archéologie Hist. 15, 41–50. https://doi.org/10.3406/valah.2013.1143.

Crabtree, G., Sarrao, J., Alivisatos, P., Barletta, W., Bates, F., Brown, G., French, R., Greene, L., Hemminger, J., Kastner, M., Kay, B., Lewis, J., Ratner, M., Rollett, A., Rubloff, G., Spence, J., Tobias, D., Tranquada, J., 2012. From quanta to the continuum: Opportunities for mesoscale science. Department of Energy, Office of Science, Basic Energy Sciences, U.S.

Daneels, A., Romo De Vivar-Romo, A., Linares-Jurado, A., Reyes-Lezama, M., Tapia-Mendoza, E., Morales-Puente, P., Cienfuegos-Alvarado, E., Otero-Trujano, F.J., 2018. Chemical analysis of bitumen paint on classic period Central Veracruz ceramics, Mexico. J. Archaeol. Sci. Rep. 17, 657–666. https://doi.org/10.1016/j.jasrep.2017.12.006.

D'Errico, D., 2019. Chipped stone artifacts: use-wear analysis. In: Romano, L., D'Agostino, F. (Eds.), Abu Tbeirah Excavations I. Area 1. Last Phase and Building A – Phase 1. Sapienza University Press, Rome, pp. 457–462.

Dutoit, C.E., Binet, L., Vezin, H., Anduze, O., Lattuati-Derieux, A., Gourier, D., 2022. Insight into the structure of black coatings of ancient Egyptian mummies by advanced electron magnetic resonance of vanadyl complexes. Magn. Reson. 3, 111–124. https://doi.org/10.5194/mr-3-111-2022.

Festa, G., Scatigno, C., Caruso, V., Giampaolo, S., Tufari, A., Ferguson, L., Greco, A., Manclossi, F., Romano, L., 2025. A kernel classifier approach to the spectroscopic classification of archaeological bitumen composites in Ancient Mesopotamia. J. Compos. Sci. under review.

Ferrant, M., Caffy, I., Cortopassi, R., Delque-Količ, E., Guichard, H., Mathe, C., Thomas, C., Vieillescazes, C., Bellot-Gurlet, L., Quiles, A., 2022. An innovative multi-analytical strategy to assess the presence of fossil hydrocarbons in a mummification balm. J. Cult. Herit. 55, 369–380. https://doi.org/10.1016/j.culher.2022.04.007.

Fulcher, K., Budka, J., 2020. Pigments, incense, and bitumen from the New Kingdom town and cemetery on Sai Island in Nubia. J. Archaeol. Sci. Rep. 33, 102550. https://doi.org/10.1016/j.jasrep.2020.102550.

Hauck, T.C., Connan, J., Charrié-Duhaut, A., Le Tensorer, J.-M., Sakhel, H.A., 2013. Molecular evidence of bitumen in the Mousterian lithic assemblage of Hummal (Central Syria). J. Archaeol. Sci. 40, 3252–3262. https://doi.org/10.1016/j.jas.2013.03.022.

Hubert, M., Rousseeuw, P.J., Vanden Branden, K., 2005. ROBPCA: a new approach to robust principal component analysis. Technometrics 47 (1), 64–79. https://doi.org/10.1198/004017004000000563.

Jing, H., Dan, H., Shan, H., Liu, X., 2023. Investigation on three-dimensional void mesostructures and geometries in porous asphalt mixture based on computed tomography (CT) images and Avizo. Materials 16, 7426. https://doi.org/10.3390/ma16237426.

Koyun, A.N., Zakel, J., Kayser, S., Stadler, H., Keutsch, F.N., Grothe, H., 2021. High resolution nanoscale chemical analysis of bitumen surface microstructures. Sci. Rep. 11, 13554. https://doi.org/10.1038/s41598-021-92835-3.

Ma, G., Yue, X., 2022. An improved whale optimization algorithm based on multilevel threshold image segmentation using the Otsu method. Eng. Appl. Artif. Intel. 113, 104960. https://doi.org/10.1016/j.engappai.2022.104960.

Manclossi, F., Romano, L., 2024. Flint sickles from South Mesopotamia: a note on their unexplored potential for understanding 3rd millennium BC people's life. Rivista Degli Studi Orientali 97 (4), 177–182. https://doi.org/10.19272/202403804010.

Mashaan, N., Karim, M., Khodary, F., Saboo, N., Milad, A., 2021. bituminous pavement reinforcement with fiber: a review. Civil Eng. 2, 599–611. https://doi.org/10.3390/civileng2030033.

Middendorf, M., Umbach, C., Böhm, S., Liu, J., Middendorf, B., 2023. Comparative study of 2D petrographic and 3D X-ray tomography investigations of air voids in asphalt. Materials 16, 1272. https://doi.org/10.3390/ma16031272.

Greco, A., Romano L., Festa, G., Caruso, V., Scatigno, C., Giampaolo, S., Tufari, A., Ferguson, L., Santarelli, M.L. forthcoming. A recipe for Reuse: From Extraction to Recycling of Bitumen in Third Millennium Mesopotamia.

Moscone, D., 2019. Chipped stone artifacts: technological analysis. In: Romano, L., D'Agostino, F. (Eds.), Abu Tbeirah Excavations I. Area 1. Last Phase and Building A – Phase 1. Sapienza University Press, Rome, pp. 439–453.

Nissenbaum, A., Rullkötter, J., Yechieli, Y., 2002. Are the curative properties of 'black mud' from the Dead Sea due to the presence of bitumen (asphalt) or other types of organic matter? Environ. Geochem. Health 24, 327–335. https://doi.org/10.1023/A:1020559717754.

Oxilia, G., Fiorillo, F., Boschin, F., Boaretto, E., Apicella, S.A., Matteucci, C., Panetta, D., Pistocchi, R., Guerrini, F., Margherita, C., Andretta, M., Sorrentino, R., Boschian, G., Arrighi, S., Dori, I., Mancuso, G., Crezzini, J., Riga, A., Serrangeli, M.C., Vazzana, A., Salvadori, P.A., Vandini, M., Tozzi, C., Moroni, A., Feeney, R.N.M., Willman, J.C., Moggi-Cecchi, J., Benazzi, S., 2017. The dawn of dentistry in the late upper Paleolithic: an early case of pathological intervention at Riparo Fredian. Am. J. Phys. Anthropol. 163, 446–461. https://doi.org/10.1002/ajpa.23216.

Pinto, J., Sanz-Minguez, C., Prieto, A.C., 2019. Presence and applications of bituminous materials on the ancient vaccaei culture: a nondestructive spectroscopic study. IMEKO TC-4 International Conference on Metrology for Archaeology and Cultural Heritage Florence.

PyCharm 2024.3.3. https://www.jetbrains.com/pycharm/, last open December 2025.

Rasheed, M.T., Guo, G., Shi, D., Khan, H., Cheng, X., 2022. An Empirical study on retinex methods for low-light image enhancement. Remote Sens. 14, 4608. https://doi.org/10.3390/rs14184608.

Romano, L., D'Agostino, F., 2019. Abu Tbeirah excavation I. Area 1. Last phase and building a – phase 1. Sapienza University Press.

Romano, L., D'Agostino, F., 2023. Abu Tbeirah: preliminary report on the 2018–2019 excavations. In: Marchetti, N., et al. (Eds.), Proceedings of the 12th International Congress on the Archaeology of the Ancient Near East, Vol. 2, 06–09 April 2021, Bologna. Harrassowitz Verlag, Wiesbaden, pp. 549–558.

Schneider, C.A., Rasband, W.S., Eliceiri, K.W., 2012. Fiji: an open-source platform for biological-image analysis. Nat. Methods 9 (7), 676–682.

Schwartz, M., Hollander, D., 2016. The Uruk expansion as dynamic process: a reconstruction of Middle to late Uruk exchange patterns from bulk stable isotope analyses of bitumen artifacts. J. Archaeol. Sci. Rep. 7, 884–899. https://doi.org/10.1016/j.jasrep.2016.01.027.

Schwartz, M., Hollander, D., 2008. Bulk stable carbon and deuterium isotope analyses of bitumen artifacts from Hacinebi Tepe, Turkey: reconstructing broad economic patterns of the Uruk expansion. J. Archaeol. Sci. 35, 3144–3158. https://doi.org/10.1016/j.jas.2008.06.021.

Schwartz, M., Hollander, D., 2000. Annealing, distilling, reheating and recycling: bitumen processing in the Ancient Near East. Paléorient 26, 83–91. https://doi.org/10.3406/paleo.2000.4712.

Stol, M., 2012. Bitumen in ancient Mesopotamia. The textual evidence. Bibliotecha Orientalis 1–2, 48–60.

Taheri-Shakib, J., 2023. A review of microstructure characterization of asphalt mixtures using computed tomography imaging: prospects for properties and phase determination. Constr. Build. Mater. 16, 7426. https://doi.org/10.3390/ma16237426.

Verderame, L. 2025. Nautica Sumerica: An Unpublished Ur III Document and the Problem of Reconstructing Ancient Watercrafts. In: Chambon, G.; Vita, J.-P. (eds.), People, Places and Technology in the Ancient Near East. Festschrift for Ariel M. Bagg (Dubsar 38). Münster: Zaphon, pp. 309–336. ISBN 978-3-96327-306-3 (print), 978-3-96327-307-0 (e-book).

Yoo, J.H., Ohm, S.Y., Chung, M.G., 2012. Brightness preservation and image enhancement based on maximum entropy distribution. In: Convergence and Hybrid Information Technology. Springer. Berlin/Heidelberg, Germany, pp. 365–372.